NAVIER-STOKES/DIRECT SIMULATION MONTE CARLO MODELING OF SMALL COLD GAS THRUSTER NOZZLE AND PLUME FLOWS

by

Richard A Nanson III

A Thesis
Submitted to the Faculty
of the
WORCESTER POLYTECHNIC INSTITUTE
in partial fulfillment of the requirements for the
Degree of Master of Science
in
Mechanical Engineering
by

____

April 2002

APPROVED:

____

Dr. Nikolaos A. Gatsonis, Advisor
Mechanical Engineering Department

____

Dr. David Olinger, Committee Member
Mechanical Engineering Department

____

Dr. John Blandino, Committee Member
Mechanical Engineering Department

____

Dr. Michael Demetriou, Graduate Committee Representative
Mechanical Engineering Department

Abstract

This study involves the modeling of small cold-gas (N_2) thrusters nozzle and plume flows, their interactions with spacecraft surfaces and the induced pressure environment. These small cold-gas thrusters were used for pitch, yaw and roll control and were mounted on the bottom of the conical Environmental Monitor Payload (EMP) suborbital spacecraft. The pitch and yaw thrusters had 0.906 mm throat diameter and 4.826 mm exit diameter, while the roll thrusters had 1.6 mm throat diameter and 5.882 mm exit diameter. During thruster firing, at altitudes between 670 km and 1200 km, pressure measurements exhibited non-periodic pulses (Gatsonis et al., 1999). The pressure sensor was located inside the EMP and was connected to it's sidewall with a 0.1-m long, 0.022-m diameter tube and the pressure pulses appeared instantaneously with the firings for thrusters without a direct line-of-sight with the sensor entrance. Preliminary analysis showed that the plume of these small EMP thrusters undergoes transition from continuous to rarefied. Therefore, nozzle and plume simulations are performed using a combination of Navier-Stokes and Direct Simulation Monte Carlo codes.

This study presents first a validation of the Navier-Stokes code Rampant used for the continuous EMP nozzle and plume simulations. The first Rampant validation example involves a two-dimensional axisymetric freejet expansion and is used to demonstrate the use of Bird's breakdown parameter. Results are compared favorably with those of Bird (1980) obtained through the method of characteristics. The second validation example involves three-dimensional plume simulations of a NASA thruster.

This nitrogen nozzle has a throat diameter of 3.18 mm, an exit diameter of 31.8 mm, half-angle of 20 degrees, stagnation temperature of 699 K, stagnation pressure of 6,400 Pa. Simulation results are compared favorably with previous Navier-Stokes and Direct Simulation Monte Carlo numerical work. The third validation example involves three-dimensional simulations of Rothe's (1970) nozzle that has a throat diameter of 2.5 mm, an exit diameter of 20.3 mm, half-angle of 20 degrees, operating at stagnation temperature of 300 K and pressure of 1975 Pa. Numerical results also compared favorably to experimental data.

The combined Navier-Stokes/DSMC approach and the EMP simulation results are presented and discussed. The continuous part of the EMP nozzle and plume flow is modeled using the three-dimensional Navier-Stokes Rampant code. The Navier-Stokes domain includes the geometry of the nozzle and the EMP base until transition of the continuous flow established by Bird's breakdown parameter. The rarefied part of the plume flow is modeled using the Direct Simulation Monte Carlo code DAC. Flowfield data obtained inside the breakdown surface from the Navier-Stokes simulation are used as inputs to the DSMC simulations. The DSMC domain includes the input surface and the EMP spacecraft geometry. The combined Navier-Stokes/DSMC simulations show the complex structure of the plume flow as it expands over the EMP surfaces. Plume reflection and backflow are demonstrated. The study also summarizes findings presented by Gatsonis et al. (2000), where the DSMC predictions at the entrance of the pressure sensor are used as inputs to a semi-analytical model to predict the pressure inside the sensor. It is shown that the pressure predictions for the pitch/yaw thrusters are

close to the measurements. The plume of a pitch or yaw thruster reaches the pressure sensor after expanding on the EMP base. The pressure predicted for the roll thruster is larger that the measured. This is attributed to the uncertainty in the roll thruster location on the EMP base resulting, in the simulation, in a component of direct flow to the sensor.

Acknowledgments

I would like to start by thanking Professor Nikos Gatsonis for all the time he has spent working with me in my course work, projects, and my Master Thesis. Additionally I would like to thank Jay Lebeau at the NASA Goddard Space Flight Center for providing simulation software as well as his time helping this project; his guidance and resources proved invaluable.

Thanks also go to my friends who listened to me grumble during those times when the project did not progress as smoothly as planned. I would like to thank my wife Roxanne for the motivation and support that she provided over the years. She has seen the beginning and the completion of this project though the duration was longer than expected.

I would lastly like to thank my family without who’s support over the years, not just during this Master Thesis, I would not be the person I am today. Their understanding that a strong education is key to the future of any person’s life has helped me to find a clear path that I can be proud of.

Table of Contents

Abstract i

Acknowledgments iv

Table of Contents v

List of Figures viii

List of Tables xiii

Nomenclature xiv

Chapter I: Introduction 1
- 1.1 Review of Small Thruster Nozzle and Plume Flow 4
- 1.2 Review of Nozzle and Plume Flow Studies 8
- 1.3 Combined 3D CFD/DSMC Methodology 13
- 1.4 Problem Statement, Objectives and Methodology 13

Chapter II 18

Navier-Stokes and DSMC Numerical Methodologies 18
- 2.1 Navier-Stokes Methodology and the Rampant Code 19
  - 2.1.1 Compressible Navier-Stokes Equations 19
  - 2.1.2 Grid Generation 20
  - 2.1.3 Finite Volume Discretization 21
  - 2.1.4 Time Integration 23
  - 2.1.5 Boundary Conditions 24
- 2.2 Navier-Stokes Code Validation 26
  - 2.2.1 Axisymmetric Plume Simulation and Comparison to Numerical Data 26
  - 2.2.2 Three Dimensional Nozzle/Plume Flow Simulation and Comparison to Numerical Data 30

2.2.3 Three-Dimensional Nozzle Flow and Comparison to Experimental Data 34

2.3 DSMC Methodology and the DAC code 38

2.3.1 Grid Generation 38

2.3.2 Boundary Conditions 39

2.3.3 DAC Flow chart 40

2.3.4 Collision Models in DAC 41

2.3.5 Time Stepping and FNUM's 41

Chapter III 43

EMP Nozzle and Plume Flow 43

3.1 EMP Description and Problem Definition 43

3.2 Numerical Methodology 48

3.3 Continuous Nozzle and Plume Flows 49

3.4 Rarefied Plume Flow 53

3.5 Results and Discussion 55

3.5.1 Pitch and Yaw Thrusters 55

3.5.2 Roll Thrusters 60

3.6 Data Comparison 65

3.7 Roll Thrusters – Second Case 69

3.8 Data Comparison –Roll Thruster Cases 74

Chapter IV 78

Summary, Conclusions and Future Work 78

4.1 Numerical Methods and Validation 79

4.2 EMP Simulations 81

4.3 Future Work 82

Reference List 83

List of Figures

Figure 1.1 EMP Geometry and Thruster Locations (*Gatsonis et al.*, 2000). 2

Figure 1.2 EMP Pressure Measurements (*Gatsonis et al.*, 1997). 3

Figure 1.3 Typical Nozzle and Plume Flow Regimes of a Small Thruster. 6

Figure 2.1 Plume geometry and results from *Bird* (1980). 27

Figure 2.2 Mach contours of an axisymmetric plume simulation using Rampant. 28

Figure 2.3 Contours of P/Kn_e of an axisymmetric plume simulation. 29

Figure 2.4 Contours of Breakdown Parameter P of an axisymmetric plume simulation. 30

Figure 2.5 DSMC and VNAP2 Mach number contours in the NASA Lewis nozzle (*Tartibini, et al., 1995*). 31

Figure 2.6 Rampant Mach number contours in the NASA Lewis nozzle. 32

Figure 2.7 NASA Lewis nozzle exit velocity profiles along radial direction. 33

Figure 2.8 NASA Lewis nozzle exit temperature profiles. 34

Figure 2.9 Nozzle geometry from Rothe experiment (1970). 35

Figure 2.10 Normalized temperature along the centerline of Rothe's nozzle. 36

Figure 2.11 Normalized pressure along the centerline of Rothe's Nozzle. 36

Figure 2.12 Normalized density along centerline of Rothe's nozzle. 37

Figure 3.1 Approximate EMP altitude and speed (*Gatsonis et al.*, 2000). 45

Figure 3.2 EMP base showing thruster location (looking forward, -Y Direction) (*Gatsonis et al.*, 2000). 45

Figure 3.3 EMP data showing the reduced pressure for the 840-860 s thruster-firing period (*Gatsonis et al.*, 1999). 46

Figure 3.4a) N-S computational domain for nozzle and plume flow. The EMP base is shown as a shaded region. The thruster is located at $(x = 0, y = 0.0184, z = 0)$ and is firing in the +X-direction. 50

Figure 3.4b) Expanded view of the N-S grid showing the nozzle and near-exit area on the (x,y,z=0) plane. The thruster is located at $(x = 0, y = 0.0184, z = 0)$ and is firing in the +X-direction. 51

Figure 3.5) N-S computational domain for roll nozzle and plume flow. The EMP base is shown as a shaded region. The roll thruster is located at $(x = 0, y = 0.0184, z = 0)$ and is firing in the +Z-direction. 52

Figure 3.6a) DSMC computational domain for the Yaw/Pitch thruster showing the EMP surface and the DSMC input surface obtained from the N-S simulations. The thruster is located at $(x = 0, y = 0.0184, z = 0)$ and is firing in the +X-direction. 54

Figure 3.6b) DSMC computational domain for the roll thruster showing the EMP surface and the DSMC input surface obtained from the N-S simulations. The roll thruster is located at $(x = 0, y = 0.0184, z = 0)$ and is firing in the +Z-direction. 54

Figure 3.7a) Number density contours (m^{-3})... 56

Figure 3.7b) Temperature contours (K). 57

Figure 3.7c) Mach contours. 57

Figure 3.7 Pitch (yaw) nozzle and plume flowfield from N-S simulations on the (x,y,z=0) plane. (Left) Expanded view of the nozzle and near-exit flow region (Right) Entire domain.. 57

Figure 3.8 Breakdown parameter contours for Pitch (or Yaw) thruster plume from N-S simulation on the (x,y,z=0) plane. 58

3.9a) Three-dimensional view. 59

3.9b) Perpendicular thruster plane (x,y,z=0). 59

3.9c) Parallel thruster plane (x,y=0.0184 ,z). 59

3.9d) Pressure sensor plane (x,y=-0.15,z). 59

Figure 3.9 DSMC number density (m^{-3}) for a pitch (or yaw) thruster plume. The thruster is located at (x=0,y=0.0184,z=0) and is firing in the +X-direction. The DSMC input surface is shown as a black-shaded region. 59

Figure 3.10 DSMC predicted surface pressure (Pa) due to Pitch (or Yaw) thruster plume. The thruster is located at (x=0,y=0.0184,z=0) and is firing in the +X-direction. 60

3.11a) Number density contours (m^{-3}). 61

3.11b) Temperature contours (K). 62

3.11c) Mach contours. 62

Figure 3.11 Roll nozzle and plume flow field from N-S simulations on the (x,y,z=0) plane. (Left) Expanded view of the nozzle and near-exit region, (Right) Entire domain. 62

Figure 3.12 Roll nozzle and plume breakdown parameter from N-S simulations shown on the (x,y,z=0) plane. 63

3.13a) Three-dimensional view. 64

3.13b) Perpendicular thruster plane (x=0,y,z). 64

3.13c) Parallel thruster plane (x, y=0.0184, z). 64

3.13d) Pressure sensor plane (x, y=-0.15, z). 64

Figure 3.13 DSMC number density (m^{-3}) for Roll thruster plume. The thruster is located at (x=0,y=0.0184,z=0) and is firing in the +Z-direction. The DSMC input surface is shown as a black-shaded region. 64

Figure 3.14 DSMC predicted surface pressure (Pa) due to Roll thruster plume. The thruster is located at (x=0,y=0.0184,z=0) and is firing in the +Z-direction. 65

Figure 3.15 Schematic of the EMP pressure-sensor (*Gatsonis et al.*, 1997). 66

Figure 3.16 Comparison of Numerical and Experimental Pressure for EMP Thrusters. Roll thruster position correspond to Case-1 68

3.17a) Number density contours (m^{-3}). 70

3.17b) Temperature contours (K). 71

3.17c) Mach contours. 71

Figure 3.17 Roll nozzle and plume flowfield from N-S simulations on the (x,y,z=0) plane. (Left) Expanded view of the nozzle and near-exit region, (Right) Entire domain. 71

Figure 3.18 Roll nozzle and plume breakdown parameter from N-S simulations shown on the (x,y,z=0) plane. 72

3.19a) Three-dimensional view. 73

3.19b) Perpendicular thruster plane (x=0,y,z). 73

3.19c) Parallel thruster plane (x, y=0.0184, z). 73

3.19d) Pressure sensor plane (x, y=-0.15, z). 73

Figure 3.19 DSMC number density (m^{-3}) for Roll thruster plume. The thruster is located at (x=0,y=0.0184,z=0) and is firing in the +Z-direction. The DSMC input surface is shown as a black-shaded region. 73

Figure 3.20 DSMC predicted surface pressure (Pa) due to Roll thruster plume. The thruster is located at (x=0,y=0.0184,z=0) and is firing in the +Z-direction. 74

Figure 3.21 Comparison of Numerical and Experimental Pressure for EMP Roll Thrusters for Case-1 and Case-2 Positions. 76

List of Tables

Table 1.1 Typical Thruster Specifications and Performance Parameters. 5

Table 3.1 EMP thruster characteristics. 46

Table 3.2 Reduced average pressure of individual thrusters (*Gatsonis et al.*, 1999). 48

Table 3.3 Estimates of flow conditions at thruster throat and exit. 49

Table 3.4 Flow conditions at the entrance of the sensor tube and predicted sensor-chamber pressure P_C. Roll thruster position correspond to Case-1. 67

Table 3.5 Flow conditions at the entrance of the sensor tube and predicted sensor-chamber pressure P_C due to Roll Thrusters for Case-1 and Case-2 positions. 75

Nomenclature

n_∞ = freestream number density, m^{-3}

T_∞ = freestream temperature, K

V_∞ = freestream velocity, m/s

V = Velocity of gas, m/s

u, v, w = component velocities, m/s

X, Y, Z = Environmental Monitor Package spacecraft axis

λ_∞ = mean-free path, m

μ = coefficient of viscosity, N·s/m^2

ν = collision frequency, s^{-1}

ρ = density of fluid, kg/m^3

c = speed of sound, m/s

c_p = specific heat, J/kg·^{o}K

d = molecular diameter, m

E = energy per unit mass, J/kg

F_i = gravity and body forces in component directions, N

h = enthalpy, J/kg

J = diffusion flux

k = conductivity,

Kn = Knudsen Number

m = mass, kg

M = Mach Number

n = number density, m^{-3}

P = breakdown parameter; Pressure, Pa

P_o = stagnation pressure, Pa

P_{op} = operating pressure, Pa

P_s = static pressure, Pa

R = gas constant, J/kg·^{o}K

Re = Reynolds Number

t = time, s

T_o = stagnation temperature, ^{o}K

T_s = static temperature, ^{o}K

T_w = wall temperature, ^{o}K

L = characteristic length, m

L_t = length of pressure tube, m

D_t = diameter of pressure tube, m

α = angle of attack, Degrees

γ = ratio of specific heats

τ_{ij} = stress tensors, Pa

U_1 = mean speed, m/s

P_1 = pressure outside sensor tube, Pa

T_1 = temperature outside sensor tube, Pa

P_2 = pressure inside sensor tube, Pa

T_2 = temperature inside sensor tube, Pa

S = ratio of mean speed to random speed

S_h = heat of chemical reactions, J

S_m = mass (added), kg

C_m = random speed, m/s

Chapter I: Introduction

In recent years the need for modeling of the plume flow of small cold gas thrusters on-board spacecraft has been growing. The drive to make satellites smaller and the increasing complexity and sensitivity of onboard instruments, has increased the potential for plume interaction. Plumes can contaminate and degrade sensitive spacecraft surfaces and sensors leading to problems ranging from sensor performance errors to power reduction and reduced communication capability. In addition, plume impingement on surfaces may generate undesirable forces. Solar panels and communication dishes are especially susceptible to these external forces due to their light construction. These forces can also create satellite rotations that are undesirable or create bending moments on long fragile structures like solar panels.

There have been numerous ground based experimental investigations of small thruster plumes. Numerical simulation studies of plumes have been carried out with Navier-Stokes codes. The major shortcomings of the continuous description of the expanding plume are related to the breakdown and non-equilibrium due to the rarefaction effects which have been addressed with the Direct Simulation Monte Carlo (DSMC) method. Recent studies have combined the two methods by following the flow via a Navier-Stokes approach until breakdown is established, then continuing with a DSMC approach.

This study involved modeling of the nozzle and plume flow of cold gas attitude control thrusters used onboard the Environmental Monitoring Package (EMP) spacecraft. The mission was conducted by the Applied Physics Laboratory to study the induced environment around a suborbital spacecraft. Eight N_2 cold gas thrusters were employed in the EMP, for pitch, yaw and roll control. The location of the thrusters is shown in Figure 1.1. A pressure sensor was used to monitor the local environment created during thruster firings. The pressure sensor was located inside the EMP on a plane 15 cm from the base of the spacecraft as shown in Figure 1.1. Pressure profile data for the duration of the EMP flight from 500 to 1620 seconds is shown in Figure 1.2.

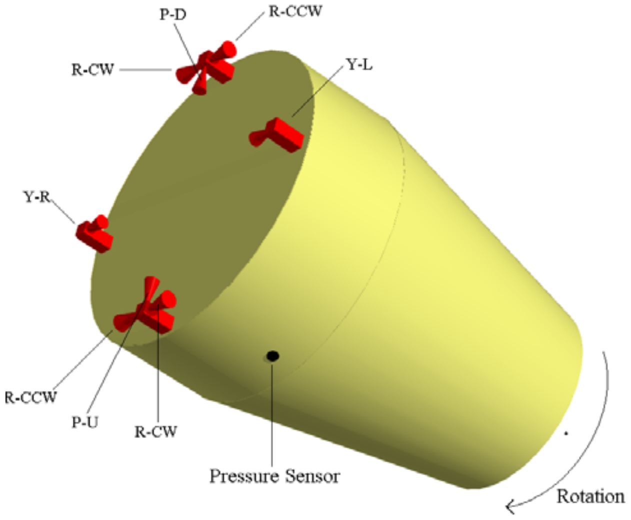

Figure 1.1 EMP Geometry and Thruster Locations (*Gatsonis et al.*, 2000).

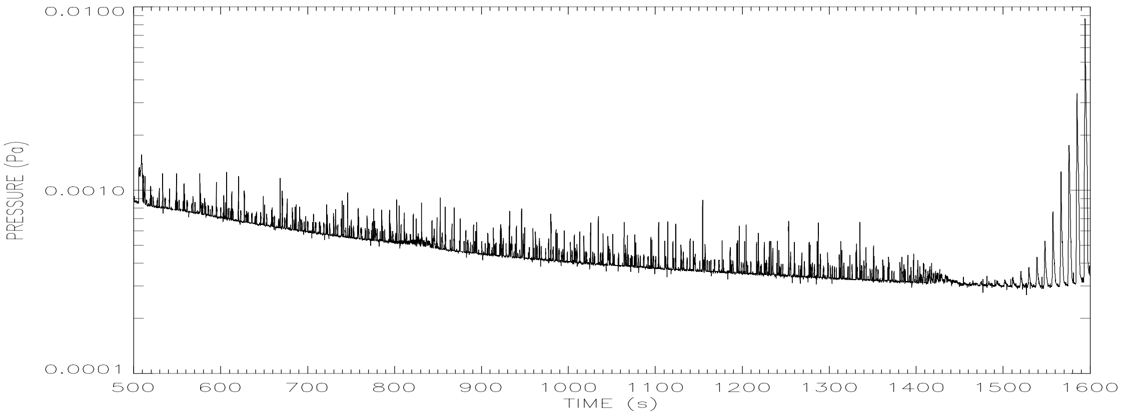

Figure 1.2 EMP Pressure Measurements (*Gatsonis et al.*, 1997).

The pressure spikes from 500 to 1400 seconds shown in Figure 1.2 have been associated with thruster firings by *Gatsonis et al.* (1999). The pressure oscillations from 1500 to 1600 seconds are associated with the ram/wake phase of the EMP mission (*Gatsonis et al.,* 1997). During the period between 500 and 1400 seconds the thrusters were fired with multiple impulses of 0.03 seconds each in duration and the complete data analysis is presented by *Gatsonis et al*. (1999).

The objectives of this study are to develop and validate a combined three-dimensional Navier-Stokes/DSMC computational approach using existing codes. Validation of the codes was performed against previous numerical and experimental work. In addition a Navier-Stokes/DSMC coupling methodology at the breakdown surface was developed and the combined methodology applied to study the EMP nozzle and plume flows.

1.1 Review of Small Thruster Nozzle and Plume Flow

Spacecraft need onboard propulsion for orbit changes and attitude control. The simplest form of chemical onboard propulsion is the cold gas thruster. The thrust is generated when a high-pressure gas expands through a nozzle. Cold gas thrusters have small (specific impulse) Isp's (approximately 70 seconds) and are not efficient. However because these systems are unheated they consume very little power which makes them easy to use and to implement at low cost.

A second class of onboard propulsion are electro-thermal thrusters which include arcjets and resistojets. These thrusters work in a similar manner to the cold gas thrusters but have the advantage of a high temperature working fluid. The increase in temperature can be achieved through many different manners such as direct electric heating or the use of heating elements. The use of high temperature fluid increases the system cost, power requirements and complexity but also increases the specific impulse up to six to tens times that of a cold gas thruster (*Brown*, 1996). This is a substantial savings when considering the high cost to launch fuel into orbit.

A third class of onboard propulsion is the electrostatic/electromagnetic propulsion thrusters (EPT) which include ion thrusters, Hall (or SPT) thrusters and pulsed plasma thrusters (PPT). In general EP thrusters accelerate ionized particles or plasma through the use of electrostatic or electromagnetic fields to very high velocities. Electric propulsion thrusters have Isp's well above 1000 seconds but the deliver relatively low thrusts.

A comparative table between various onboard thrusters is shown bellow in Table 1.1 (*Brown*, 1996)

Type	Propellant	Energy	Thrust (N)	Isp (Sec)
Cold Gas	N_2	Pressure	0.05-200	50-75
Resistojet	N_2, NH_3, etc	Resistive Heat	0.005-0.5	150-700
Arcjet	NH_3, H_2, etc	Elec. Arc Heat	0.05-5	450-1500
Ion	Hg/A/Xe/Cs	Electrostatic	5E-6 – 0.5	2000-6000
Pulsed Plasma	Teflon	Electromagnetic	5E-6 -0.005	1500

Table 1.1 Typical Thruster Specifications and Performance Parameters.

This thesis investigates cold gas thrusters and as such we will review some interesting features that occur as the flow progresses from the nozzle throat to the nozzle exit. These features include the formation of a boundary layer in the nozzle, rapid expansion as the flow travels past the nozzle lip at the exit, and a plume flow that may begin as continuous and reach a rarefied state further downstream. A general schematic of the process is shown in Figure 1.3.

Boundary layer effects play an important role in determining the nozzle and plume flow characteristics of cold gas thrusters. Due to the very small diameter of these nozzles, the boundary layer can occupy a significant portion of the nozzle diameter. One of the parameters used to evaluate the thickness of the boundary layer is the Reynold's number given by

$$\mathrm{Re} = \frac{\rho V L}{\mu} \tag{1.1}$$

where ρ is the gas density, V is the velocity of the gas, L is the characteristic length, and μ is the viscosity of the gas. Flows with a high Re number have a less significant (thinner thickness) boundary layer with a larger isentropic core region as compared to low Re flows. High-Re flows generally occur in cold gas thrusters that have high stagnation pressures. For low Re flows the boundary layer may reach to a thickness nearly equal to that of the radius of the nozzle. The formation of a boundary layer leads to losses in efficiency and also affects the subsequent plume flow.

As the flow leaves the nozzle lip, it undergoes a rapid expansion sometimes described as a Prandtl-Meyer expansion. The expansion angle can be used to determine the size and direction of the plume that forms outside the nozzle (*Bird*, 1980).

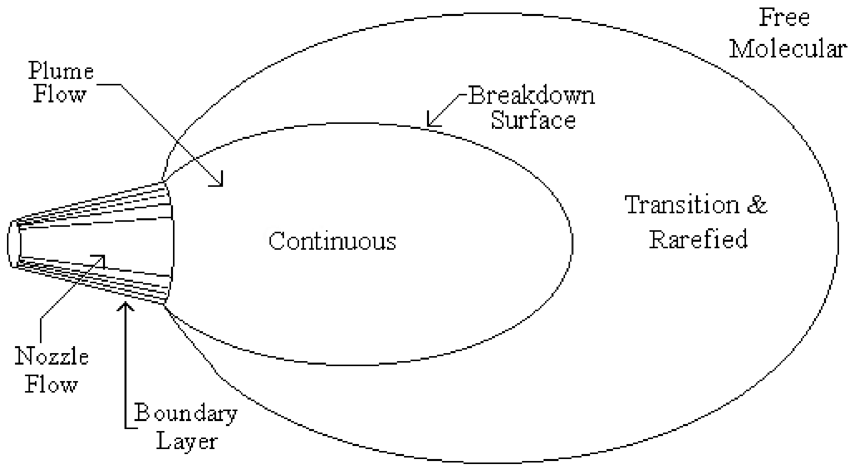

Figure 1.3 Typical Nozzle and Plume Flow Regimes of a Small Thruster.

As the plume expands the gas becomes rarefied. As long as the flow can be considered to be continuous it can be described using the Navier-Stokes equations. As rarefaction increases, the flow reaches the transitional regime and the breakdown point defined by *Bird* (1970). This point must be determined in order to evaluate the validity of Navier-Stokes based plume solutions. The breakdown is associated to the non-equilibrium state of the expanding plume flow that requires consideration of the vibrational, translational and rotational temperatures of the gas.

One criterion used to determine the breakdown point of a flowing gas is the non-dimensional Knudsen number defined as

$$Kn = \frac{\lambda}{L} \tag{1.2}$$

where L is the characteristic length of the flow. The mean-free path for elastic collisions, λ, in a simple gas is defined as

$$\lambda = \frac{1}{\sqrt{2}\pi d^2 n} \tag{1.3}$$

where d is the hard sphere molecular diameter and n is the number density of the gas. Continuous flow requires $Kn \leq 0.01$, slip flow $0.01 \leq Kn \leq 0.1$, transition $Kn \geq 0.1$ and free molecular flow $Kn \geq 10$. A better definition of the Kn may be based on a local characteristic length, which is based on macroscopic gradients of flow properties such as density. Using a local characteristic length allows the flow field to be considered continuous until the $Kn \geq 0.2$ (Bird, 1994).

In order to determine the transition point more accurately, *Bird* (1970) defined the breakdown parameter given by

$$P = \frac{1}{\nu}\left|\frac{D(\ln\rho)}{Dt}\right| \tag{1.4}$$

where ν is the collision frequency and ρ is the density of the gas. The breakdown parameter does not suffer from the problems associated with determining a local characteristic length, as it is determined primarily from the collision frequency ν and density gradients. As the flow becomes rarefied, collisions will occur less frequently and thus the value of the breakdown parameter will increase. A flow-field is considered to be in transition state for $0.03 \leq P \leq 0.05$ and is considered rarefied when $P > 0.05$. For $P > 1.0$ the flow is approximately in the free-molecular regime.

For an expanding plume flow, *P* can be used to obtain a breakdown surface as shown in Figure 1.3. Once transition has been reached a method which does not use the Navier-Stokes equations must be implemented to obtain an accurate solution. The use of Direct Simulation Monte Carlo (DSMC) method is the most common approach. DSMC developed by *Bird* (1994) is a particle based method capable of modeling rarefied gas flows in non-equilibrium.

1.2 Review of Nozzle and Plume Flow Studies

Over the past three decades a large number of studies have been performed in an attempt to better understand the behavior of thruster plume flow using experiments, analytical modeling and computations involving continuum (CFD) and rarefied methodologies (DSMC). Recently, studies involving a combination of CFD and DSMC methodologies have added significantly to our modeling capabilities as well as the understanding of these flows. Some of these works are reviewed below.

Hill and *Draper* (1966) presented some of the first analytic techniques for describing expanding plume flows into vacuum. *Bird* (1970) studied the breakdown of translational equilibrium and established the Direct Simulation Monte Carlo method. A one-dimensional empirical breakdown formula [Eq 1.4] was proposed in order to define the point at which breakdown of the continuum domain occurs. One of the most widely referenced experimental studies was performed by *Rothe* (1971) who used an electron beam technique for measurements of viscous flows in supersonic nozzles. Rothe measured the temperature and density properties of nitrogen flows along the nozzle centerline. This data set has been used very often for comparison with numerical studies. *Bird* (1980) studied the breakdown of continuum flow in Prandtl-Meyer expansions, free jets and rocket plumes using the DSMC method. *Naumann* (1988) employed a particle simulation technique to study plume flows and determine impingement parameters. This study also determined the optimal nozzle geometry that reduces plume expansion to a minimum. In *Boyd* and *Stark* (1989) the effects of the isentropic core of a thruster on plume impingement were investigated using the method of characteristics (MOC) and DSMC. *Nelson* and *Doo* (1989) used DSMC to simulate nozzle and plume flows expanding into a vacuum and compared results with experimental data. Their DSMC domain included the nozzle throat as rarefaction prevailed in most of the nozzle considered. In *Mombo-Caristan* et al. (1989) the use of laser beam deviation technique was employed in measuring freejet densities in a supersonic nozzle. The method of characteristics was also used to calculate the densities inside the nozzle for comparison with the experimental data. In *Schabrath et al*. (1989) intracavity laser scattering was used to investigate CO_2 and N_2O freejets. These experiments were performed to better understand rotational and vibrational temperatures of low density plume flows. *Campbell* (1991) used the DSMC method to study plume/free stream interactions applicable to a rocket exhaust plume at high altitudes. The numerical results compared favorably with experimental data involving pitot probes, photographs and electron beam density measurements. *Beylich et al,* (1992) performed a numerical and experimental investigation of freejets from annular orifices. Simulations were performed using a Navier-Stokes code and the numerical results were compared with pitot tube pressure and electron beam density measurements. The results were found to be comparable to data for Reynolds numbers that were over 1000. *Boyd et al*. (1992) studied the flow of small helium nozzles and plumes using DSMC and compared the numerical results with experimental data. A simple analytical model developed by *Simons* (1972) was also compared with the DSMC results for validation. *Boyd and Penko* (1992) investigated nitrogen plumes from small nozzles. They compared pitot tube pressure measurements, temperature and velocity data to simulations using continuum and DSMC methodologies. In this study the flow quickly became rarefied and the DSMC results provided a much more accurate description of the expanding flow. In *Dupuis* (1992) DSMC was used to study the plume flow and its impingement effects on control surfaces of spacecraft. *Meyer* (1992) conducted experiments to measure the particle densities of plumes expanding in a background gas. The data was used to determine the plume geometry and flowfield parameters such as temperature and velocities. *Chung* and *De Witt* (1993) using continuum and DSMC methods, studied low density nozzle flows and compared the results with experimental data of *Rothe* (1970). *Rault* (1993) presented a three-dimensional DSMC code as an efficient means of calculating plume flows around complex geometries. The calculated flows were compared against wind tunnel measurements and flight data. In *Teshima* (1993) the structure of freejets flowing from a rectangular orifice was studied through the use of laser induced fluorescence. The focus of the paper was on barrel shocks that form from different size area ratio nozzles. *Zelesnik et al*. (1993(a)) performed low-Reynolds number ($100 \leq \mathrm{Re} \leq 1000$) nozzle simulations using DSMC. The study determined performance characteristics associated with conical, trumpet and bell nozzles. *Zelesnick et al*. (1993(b)) also used DSMC methodologies to study the effects of nozzle geometry on the internal and external flow of small nitrogen thrusters. Their study included conical, trumpet and bell shaped nozzles with comparisons between helium and nitrogen gas species. *Boyd et al*. (1994 a) performed DSMC computational and experimental investigations of low density plumes of hydrogen. The experimental techniques involved Raman scattering and were used for DSMC code validation. *Boyd et al*. (1994 b) also studied micro-thruster helium flows at $0.1 \leq \mathrm{Kn} < 1$ using the DSMC method. The numerical results were also compared with experimental data. *Genkin et al*. (1994) investigated the plumes of small thrusters using the semi-inverse marching characteristics scheme (SIMA) and power-law interpolation. Simulation results were compared against three different small-plume experiments. *Gilmore et al*. (1995) studied the breakdown of continuum flows in rapidly expanding plumes and compared Navier-Stokes and DSMC solutions with experimental data gathered in a low density wind tunnel facility. They concluded that the failure of the continuum model occurs well before the translational temperature departes from the continuum value. *Tartabini et al*. (1995) used continuum and DSMC methodologies to study plume interactions with a flat plate. The nozzle flow was simulated using continuous and DSMC approaches while the plume flow was simulated using DSMC. The work by *Boyd et al*. (1996) presented numerical and experimental studies of rarefied flows from small nozzles. The studies involved hydrogen, and nitrogen plume flows using Navier-Stokes and DSMC methodologies. The numerical results were compared against the experimental data and confirmed the validity of the computational methods. In *Liang et al*. (1996) the study of low thrust nozzles was performed numerically using the method of characteristics and a Navier-Stokes code. Validation was performed against previous numerical work and experimental data. The main goal of the study was to optimize the nozzle geometry in order to improve efficiency.

Pickett et al. (1996) presented some of the few space based results from neutral gas releases onboard a suborbital vehicle. The study involved the SPEAR-3 rocket with an onboard environmental monitoring package, which measured the neutral pressure around the rocket. They identified pressure spikes associated with gas releases. Finally *Gatsonis et al.* (1998a) performed data analysis of pressure measurements during small cold gas thruster firings onboard the EMP spacecraft. This data will be reviewed further in Chapter 3 of this study.

1.3 Combined 3D CFD/DSMC Methodology

In recent years several attempts to combine continuous with rarefied approaches have appeared in the literature, in part due to increased computational power. The combined approach begins by modeling the internal flow from a thruster and if possible the plume, using continuum solvers until breakdown of the continuum assumption. Once this solution is complete, information from the continuum solution can be used as input data for a rarefied approach such as DSMC. These techniques are computationally expensive but with recent breakthroughs in computational power, studies involving combined methodologies have been becoming more frequent.

Lumpkin et al. (1995, 1996) performed combined three-dimensional numerical simulations of plume impingement using continuum and DSMC methodologies. The continuum solution was followed until breakdown and provided input data for the subsequent DSMC simulation. *Ivanov et al*. (1997) presented a similar numerical analysis of thrusters studied previously by *Rothe* (1970) and *Chung et al.* (1995) in which experimental data was available. They used a Navier-Stokes code until breakdown and initiated the DSMC simulation at the breakdown surface. *Ivanov et al.* (1998) presented a comparison study of free flight experimental results with Numerical Simulation for cold gas thruster plumes from the Mir space station.

1.4 Problem Statement, Objectives and Methodology

Through the use of CFD (continuum) and DSMC (rarefied) methodologies, a better understanding of the properties of nozzle and plume flow from small thrusters has been gained. Previous 2D and recent 3D studies have contributed considerably to our understanding of the complex non-equilibrium phenomenon associated with expanding plume flows. However there is still a need for:

1. Efficient 3D methodologies to simulate plumes and their interactions with realistic spacecraft geometries.
2. Methods that couple Navier-Stokes (continuous) and DSMC (rarefied) methodologies at the breakdown surface.
3. Code validations with space-based data since there have been very few such studies.

The Objectives of this study are:

1. Develop a combined 3D Navier-Stokes/DSMC modeling approach using existing codes to study nozzle and plume flows.
2. Validate the Navier-Stokes code with previous numerical and experimental results.
3. Develop a Navier-Stokes/DSMC coupling methodology at the breakdown surface.
4. Apply the combined methodology in the simulation of the cold gas nozzle and plume flows of the EMP spacecraft.

Methodology and Approach

The Navier-Stokes solver used in our study to simulate the continuous part of the nozzle and plume flow is Rampant 4.0, a compressible finite-volume code. Rampant is capable of simulating a wide range of flows involving heat transfer, chemical reactions, turbulent flow and complex geometries. In our simulations chemical reactions are ignored since all cases involve inert gases like helium and nitrogen. Turbulent flow modeling is also disabled since these flows experience Reynolds numbers below 5,000.

The DSMC code used in this study is DAC and was developed at the NASA Johnson Spaceflight Center (*Le Beau*, 1997). The code uses a 3D tetrahedral grid, is capable of modeling complex geometries and has a re-grid capability based on mean free path of the plume flow.

Navier-Stokes Code Validation

1) The first Rampant validation example involves a 2D axisymetric Prandtl-Meyer expansion. This case is used to demonstrate the use of Bird's breakdown parameter, *P* and the results are compared with those by *Bird* (1980).
2) The second validation example involves plume flows from the NASA Lewis Research Center nozzle of *Tartabini* et al. (1995). Three-dimensional simulation results are compared with N-S and DSMC results of *Tartabini* et al. (1995).
3) The third validation example involves three-dimensional simulations of a nozzle flow and numerical results are compared to experimental data by *Rothe* (1971).

No validation was performed for DAC as the code has been used extensively in plume studies (*Lumpkin*, 1995; *Lumpkin*, 1996).

Coupling Navier-Stokes and DSMC

In plume simulations, input conditions to the DSMC code are obtained from the N-S solution. In our study the steps involved in a nozzle/plume simulation are as follows:

1) The Navier-Stokes solution is run until convergence is achieved.
2) From this solution a breakdown surface is defined using Bird's breakdown parameter.
3) In order to use the Navier-Stokes solution data as the input boundary in the DSMC code, a grid is generated that approximates a surface inside the 3D breakdown surface found from the 3D N-S solution.
4) Using a post processing software such as TecPlot®, the data from the N-S solution is interpolated onto the input surface grid generated for the DSMC solution.
5) The DSMC code is run until a steady state solution is reached.

EMP Nozzle and Plume Flow Simulation

The N-S/DSMC methodology applied to the simulation of the EMP thrusters can be summarized as follows:

1) First, perform three-dimensional N-S simulations of the nozzle and plume flow until breakdown using a domain that includes the thruster geometry and the necessary EMP surfaces.
2) Second, perform three-dimensional DSMC simulations for the plume flow in a domain that includes the EMP geometry up to the plane of the pressure sensor. The input surface to the DSMC is inside the breakdown surface as determined by the N-S simulations.

3) Third, the N-S/DSMC predictions at the entrance of the pressure-sensor tube are used by *Gatsonis et al.* (1999) in conjunction with the theory of *Hughes and de Leeuw* (1965) to obtain the pressure inside the sensor chamber. These predictions are summarized in this study.

In Chapter II the numerical methodologies for the Navier-Stokes and DSMC methods are presented. The validation cases of the Navier-Stokes code are also presented. In Chapter III, simulations of the EMP thruster nozzle and plume flows are presented. Chapter IV presents a summary and conclusion that can be drawn from the study of the EMP thrusters.

Chapter II

Navier-Stokes and DSMC Numerical Methodologies

In this chapter the Navier-Stokes (N-S) and DSMC computational methodologies and codes used in this study are presented. Validation of Rampant, a compressible Navier-Stokes code, is accomplished by comparisons against numerical and experimental results from previous nozzle flow studies. The first Rampant validation example involves a 2D axisymetric Prandtl-Meyer expansion. This case is used to demonstrate the use of Bird's breakdown parameter, P and results are compared with data from *Bird* (1980). The second validation example involves a NASA Lewis Research Center nozzle geometry of *Tartabini et al.* (1995) Three dimensional simulation results are compared with N-S and DSMC numerical work of *Tartabini et al.* (1995). The third validation example involves three-dimensional simulations of a nozzle flow and numerical results are compared to experimental data by *Rothe* (1970).

2.1 Navier-Stokes Methodology and the Rampant Code

2.1.1 Compressible Navier-Stokes Equations

The continuum solutions in this study are obtained using Rampant, a finite volume code that solves the Navier-Stokes equations. Presented below is a summary of the computational methodology employed in Rampant.

The continuity equation in Cartesian coordinates is given by

$$\frac{\partial\rho}{\partial t}+\frac{\partial}{\partial x}(\rho u)+\frac{\partial}{\partial y}(\rho v)+\frac{\partial}{\partial z}(\rho w)=S_m \tag{2.1}$$

where ρ is the density, u, v and w are the x, y and z components of the velocity and S_m is the mass added to the domain defined by a user input.

The momentum equations are given by

$$\frac{\partial}{\partial t}(\rho u)+\frac{\partial}{\partial x}(\rho uu)+\frac{\partial}{\partial y}(\rho uv)+\frac{\partial}{\partial z}(\rho uw)=-\frac{\partial P}{\partial x}+\frac{\partial\tau_{xx}}{\partial x}+\frac{\partial\tau_{yx}}{\partial y}+\frac{\partial\tau_{zx}}{\partial z}+F_x, \tag{2.2a}$$

$$\frac{\partial}{\partial t}(\rho v)+\frac{\partial}{\partial x}(\rho vu)+\frac{\partial}{\partial y}(\rho vv)+\frac{\partial}{\partial z}(\rho vw)=-\frac{\partial P}{\partial y}+\frac{\partial\tau_{xy}}{\partial x}+\frac{\partial\tau_{yy}}{\partial y}+\frac{\partial\tau_{zy}}{\partial z}+F_y, \tag{2.2b}$$

$$\frac{\partial}{\partial t}(\rho w)+\frac{\partial}{\partial x}(\rho wu)+\frac{\partial}{\partial y}(\rho wv)+\frac{\partial}{\partial z}(\rho ww)=-\frac{\partial P}{\partial z}+\frac{\partial\tau_{xz}}{\partial x}+\frac{\partial\tau_{yz}}{\partial y}+\frac{\partial\tau_{zz}}{\partial z}+F_z, \tag{2.2c}$$

where P is the pressure, ρ is the density, τ_{ij} are components of the stress tensor and F_i are the gravity and body forces in the component directions. The stress tensor τ_{ij} is given by

$$\tau_{ij}=\left[\mu\left(\frac{\partial u_i}{\partial x_j}+\frac{\partial u_j}{\partial x_i}\right)\right]-\frac{2}{3}\mu\frac{\partial u_l}{\partial x_l}\delta_{ij}, \tag{2.3}$$

where μ is the viscosity and the second term on the right hand side is the effect of volume dilation.

Conservation of energy is written as

$$\frac{\partial}{\partial t}(\rho E)+\frac{\partial}{\partial x_i}(u_i(\rho E+p))=\frac{\partial}{\partial x_i}(k\frac{\partial T}{\partial x_i}-\sum_{j'} h_{j'}J_{j'}+u_j\tau_{ij})+S_h, \tag{2.4}$$

where E is the total energy per unit mass, k is the conductivity, h_j is the enthalpy, $J_{j`}$ is the diffusion flux of species j` and x_i denotes summation over i=1,2,3... The source term S_h includes heat of chemical reactions, any interphase exchange of heat or other volumetric heat source. The total energy E is defined as

$$E=h-\frac{p}{\rho}+\frac{u_i^2}{2} \tag{2.5}$$

Enthalpy h for an ideal mixed gas is defined as

$$h=\sum_{j'} m_{j'}h_{j'} \tag{2.6}$$

where $m_{j`}$ is the mass fraction of species j` and

$$h_{j'}=\int_{T_{ref}}^{T} c_{p,j'}dT \tag{2.7}$$

where c_p is the specific heat and T_{ref} = 298.15 K.

2.1.2 Grid Generation

An initial geometry of the computational domain is drawn using the graphics package GeoMesh. The geometry is then imported into P-Cube where nodal distribution and boundary condition assignments on the faces of the boundary surface are applied. The generated grid is based on hexahedral elements, which can then be used directly by Rampant.

To create a grid that can more closely model arbitrary shapes a surface grid can be generated in P-Cube out of triangular elements. This can be imported into T-Grid to create the unstructured tetrahedral volume mesh. T-Grid uses a Delaunay Triangulation methodology to generate the volume mesh in the domain. An initial mesh is created which contains all the boundary nodes and boundary faces. This initial mesh is then refined by placement of interior nodes until a reasonably fine mesh is generated. Once the interior volume mesh has been generated Rampant can be used to simulate a flow through the specified geometry and boundary conditions.

2.1.3 Finite Volume Discretization

Rampant uses a Finite-Volume Method (FVM) scheme for spatial discretization of the N-S equations (2.1 – 2.7). In Rampant the N-S equations are written in flux form as:

$$\Gamma \frac{\partial \boldsymbol{Q}}{\partial \mathrm{t}} + \frac{\partial \boldsymbol{F}}{\partial \mathbf{x}} = \frac{\partial \boldsymbol{G}}{\partial \mathbf{x}} \tag{2.8}$$

where Γ is a preconditioning matrix and ***Q***, ***F***, and ***G*** are flux vectors of primitive variables (*Fluent*, 1996). The governing equation in Cartesian form is integrated over an arbitrary volume, *V*, with differential surface area, ***dA***, as

$$\Gamma \frac{\partial}{\partial t} \iiint \mathbf{Q}\, dV + \iint [\mathbf{F} - \mathbf{G}]\, d\mathbf{A} = 0\,. \tag{2.9}$$

Following the finite volume spatial discretization the physical domain is subdivided into small non-deforming polyhedral cells and the integral in Eq. 2.9 is applied to each cell. Each control volume in the flow field is represented by $\tilde{\boldsymbol{Q}}$, the cell-average variable given by

$$\tilde{\mathbf{Q}} \equiv \frac{1}{V} \iiint \mathbf{Q} dV . \tag{2.10}$$

Upon substitution into Eq 2.9 it becomes

$$\Gamma \frac{\partial \tilde{\mathbf{Q}}}{\partial t} + \frac{1}{V} \iint [\mathbf{F} - \mathbf{G}] \cdot d\mathbf{A} = 0 . \tag{2.11}$$

The surface integral is evaluated by first dividing the cell surface into discrete faces and introducing the discrete flux vectors, $\tilde{\boldsymbol{F}}$ and $\tilde{\boldsymbol{G}}$. The surface integration is performed piecewise on each face assuming that the fluxes are constant across each face. The discretized system reduces to the system of differential equations

$$\Gamma \frac{\partial \tilde{\mathbf{Q}}}{\partial \boldsymbol{t}} + \frac{1}{\boldsymbol{V}} \sum_{\boldsymbol{faces}} (\tilde{\mathbf{F}} - \tilde{\mathbf{G}}) \cdot \mathbf{A} = 0 \tag{2.12}$$

where $\boldsymbol{A}$ is a face area vector.

For higher accuracy, the solution vector $\bar{\mathbf{Q}}$, used to evaluate the fluxes at cell faces is computed using a multidimensional linear reconstruction technique. This is achieved through a Taylor series expansion of the cell-average solution vector about the cell centroid

$$\bar{\mathbf{Q}} = \tilde{\mathbf{Q}} + \nabla \tilde{\mathbf{Q}} \cdot \Delta \mathbf{x} \tag{2.13}$$

where $\Delta \boldsymbol{x}$ is the displacement vector from the cell centroid to the face centroid. The gradient $\nabla \tilde{\mathbf{Q}}$ is computed using the divergence theorem, which is written as

$$\nabla\tilde{\mathbf{Q}} = \frac{1}{V}\sum_{faces}\bar{\mathbf{Q}}\mathbf{A} \tag{2.14}$$

The gradients $\nabla\tilde{\mathbf{Q}}$ are limited so that they do not introduce new maxima or minima into the reconstructed data. For first-order accuracy the face fluxes are computed from cell variables rather than using linear reconstruction. The cell face quantities are determined by assuming that the flow quantities are constant across each cell.

2.1.4 Time Integration

Rampant then proceeds with the integration of the system of ordinary differential equations described in Eq. (2.12). The general expression for the time evolution of a variable ϕ is given by

$$\frac{\partial\phi}{\partial t} = F(\phi) \tag{2.15}$$

where the function $F(\phi)$ includes the spatial discretization. Using backward differencing and a time step Δt, the first order accurate temporal discretization becomes

$$\frac{\phi^{n+1} - \phi^{n}}{\Delta t} = F(\phi) \tag{2.16}$$

and the second-order accurate discretization becomes

$$\frac{3\phi^{n+1} - 4\phi^{n} + \phi^{n-1}}{2\Delta t} = F(\phi) \tag{2.17}$$

The evaluation of $F(\phi)$ can be performed implicitly or explicitly. In the explicit time integration, $F(\phi)$ is evaluated at the current time level n as

$$\frac{\phi^{n+1}-\phi^{n}}{\Delta t}=F(\phi^{n}) \tag{2.18}$$

Explicit integration is used by Rampant when global time stepping is chosen. For a time-accurate solution, the time step in each cell in the domain must be the same. In order to maintain stability in the solution, Rampant chooses the smallest time step and applies it to the entire domain. This method is rather restrictive and is used primarily for capturing fluid flow behavior like shocks.

For steady simulations Rampant uses an implicit method to evaluate *F(ϕ)* at the new time level, *n+1*, according to

$$\frac{\phi^{n+1}-\phi^{n}}{\Delta t}=F(\phi^{n+1}) \tag{2.19}$$

2.1.5 Boundary Conditions

Inlets and outlets of the flows as well as walls require implementation of boundary conditions. Rampant defines them as pressure inlet and outlet boundaries.

Pressure Inlet Boundaries

The boundary conditions necessary to compute the inlet conditions are the total pressure, P_o, static pressure, P_s, and the total temperature, T_o. From these input conditions the velocity of the flow at the inlet is computed from the following relation

$$\frac{P_o}{P_s}=\left[1+\frac{\gamma-1}{2}M^2\right]^{\frac{\gamma}{\gamma-1}}. \tag{2.20}$$

The Mach number, M is defined as

$$M = \frac{v}{c} = \frac{v}{(\gamma R T_s)^{1/2}} \tag{2.21}$$

where, c is the speed of sound, γ is the specific heat of the fluid and R is the gas constant. The static temperature T_s is computed from

$$\frac{T_o}{T_s} = 1 + \frac{\gamma - 1}{2} M^2 \tag{2.22}$$

and the density at the inlet plane for an ideal gas is given by

$$\rho = P_s \ / \ R T_s \tag{2.23}$$

Pressure Outlet

A static pressure is specified as the outflow boundary condition at the exit. This is only used as long as the flow remains subsonic. If the flow becomes supersonic then the exit conditions are extrapolated from the internal upstream flow conditions using Riemann invariants.

A set of backflow conditions are also utilized by Rampant in cases where the flow is reversed at the pressure outlet during the solution process. These backflow conditions require specification of total stagnation temperature.

Wall Boundaries

Wall boundary conditions can be of three different types in Rampant.

Fixed Heat Flux: The default is an adiabatic wall condition in which zero heat flux to the wall occurs. A heat flux to the wall must otherwise be specified.

Fixed Temperature: A constant wall temperature is specified.

Convective Heat Transfer: Heat transfer from the fluid stream to the wall is calculated.

2.2 Navier-Stokes Code Validation

A series of two and three dimensional nozzle and plume simulations are performed in order to validate the Rampant code.

2.2.1 Axisymmetric Plume Simulation and Comparison to Numerical Data

The first case used for the validation of Rampant is an axially symmetric freejet expansion near a wall lip. Though this case is also useful for the validation of the 2D axisymmetric code, the primary objective is to demonstrate the use of Bird's breakdown parameter, P, in determining the point at which the continuum solver can no longer be applied.

Figure 2.1 shows the geometry of the freejet used by *Bird (1980)*. Bird used the method of characteristics (MOC) to calculate the plume flow of a diatomic gas and uniform conditions with M=1.1. The simulation domain is set up using a stagnation pressure of P_o=10130 Pa and a temperature of T_o=300^o K. The flow inlet boundary condition is set at to a constant velocity with M=1.1, the gas is taken as N_2 and the simulation is performed assuming laminar flow conditions. For this case the Knudsen number at the exit is approximately 0.05 and the rarefaction of the flow takes place only near the nozzle lip backflow region or at large distances from the exit of the jet *(Bird, 1980)*.

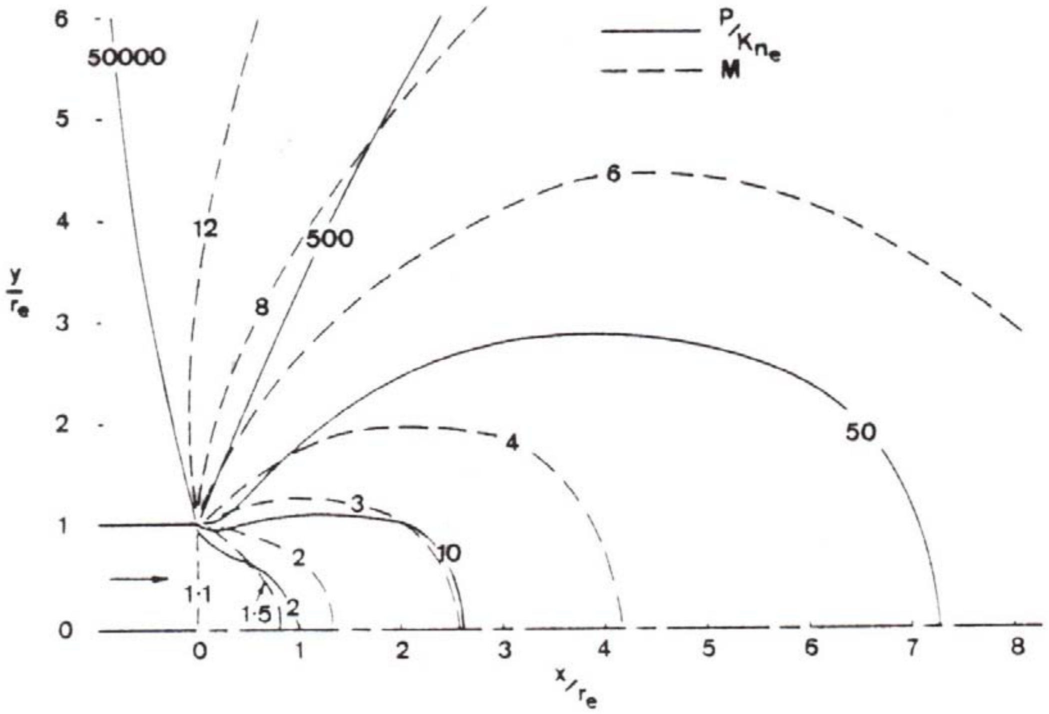

Figure 2.1 Plume geometry and results from *Bird* (1980).

The axes in the Bird (1980) results in Figure 2.1 are non-dimensionalized to the radius of the freejet nozzle exit. The Rampant results in Figure 2.2, Figure 2.3 and Figure 2.4 are actual distances in meters. The x=1 corresponds to the $x/r_e=5$ distance in Figure 2.1.

In Figure 2.1 and Figure 2.2, contours of Mach number are presented for Bird (1980) and our Rampant simulation and demonstrate an overall good agreement. One discrepancy between the two results is that the Mach contours from Bird are all connected to the wall lip while the contours in the Rampant solution are detached for the higher Mach values. This is a result of the breakdown of the continuum flow near the external wall lip of the freejet.

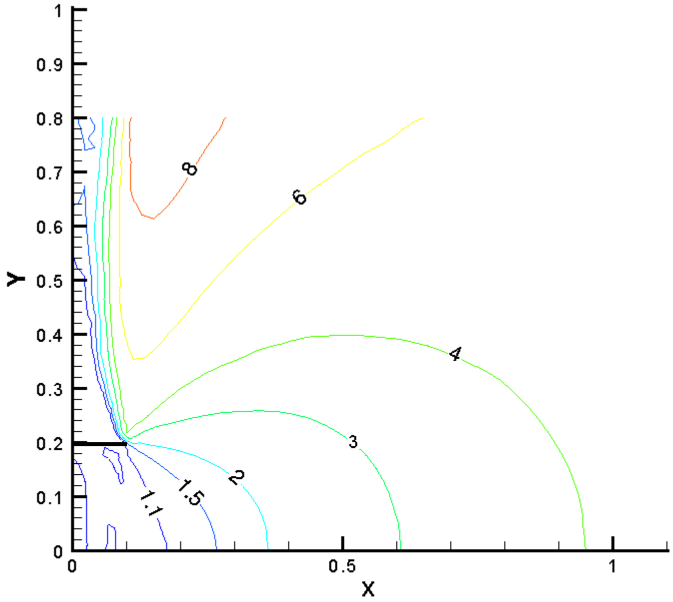

Figure 2.2 Mach contours of an axisymmetric plume simulation using Rampant.

Figure 2.3 displays contour ratios of breakdown parameter to Knudsen number P/Kn_e. This is a means of determining if the flow field is within the continuum domain. The values of Kn_e are based on the characteristic length of the nozzle radius. Once again the comparison with the data from Bird in Figure 2.1 shows agreement with results obtained from the Rampant solution. The P/Kn_e contours of 50 and 500 correspond to Knudsen values of 10^{-3} and 10^{-4} respectively *(Bird, 1980)* indicating that the plume flow is within the continuous regime and, thus, can be simulated using a Navier-Stokes solver such as Rampant.

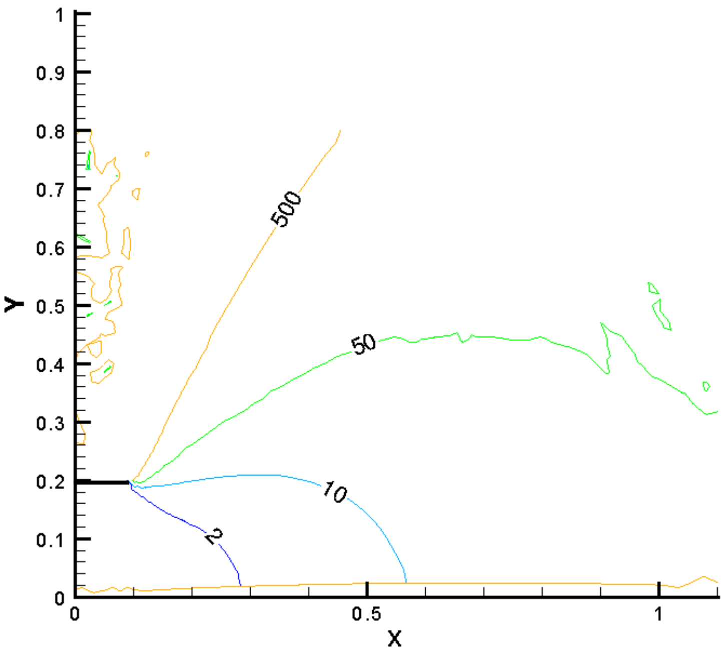

Figure 2.3 Contours of *P*/Kn$_e$ of an axisymmetric plume simulation.

Figure 2.4 presents contours of breakdown parameter, *P* and shows that most of the plume has values of $P<0.01$. It is generally accepted that transition flow starts at $P \cong 0.3$, while rarefied flow begins at $P \cong 0.5$ (Bird, 1994). Therefore it can be concluded that the plume for the most part is continuous. Figure 2.4 shows that a small area adjacent to the lip has a $P=0.03$. Since transitional flow and breakdown are beginning to occur at this point, it is not possible to completely accept the N-S solution in this area. The Mach number contours in the near-lip area of Figure 2.2 also demonstrate that the breakdown of the continuous flow can adversely affect the N-S solution.

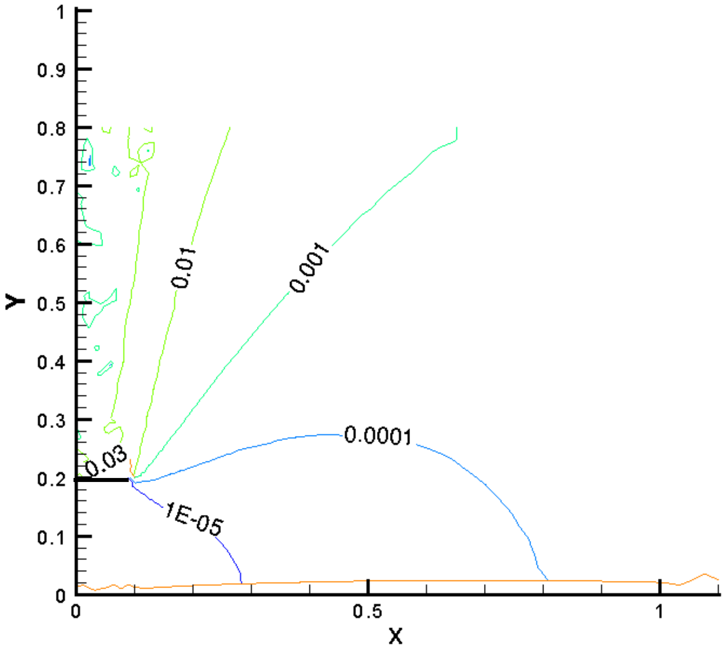

Figure 2.4 Contours of Breakdown Parameter *P* of an axisymmetric plume simulation.

2.2.2 Three Dimensional Nozzle/Plume Flow Simulation and Comparison to Numerical Data

This case is used to validate the use of the Rampant code in a 3D flow by comparison with the numerical results of *Tartabini et al.* (1995). These authors used a NASA Lewis nozzle and compared N-S (VNAP2 code) to DSMC (G2 code) simulation results. The nozzle has a throat diameter of 3.18 mm and an exit diameter of 31.8 mm with a 20^{o} half angle. The stagnation pressure and temperature are 6,400 Pa and 699^{o} K respectively and the test gas is nitrogen. A no-slip boundary condition is enforced at the wall, with a wall temperature of 545^{o} K. The Reynolds number at the exit is Re=850, and the Kn at the exit is approximately 0.02. Under these conditions the flow rarefies near the nozzle exit causing the Navier-Stokes solution to become invalid. Mach contours from *Tartabini et al.* (1995) presented in Figure 2.5, show the differences between the N-S and DSMC solutions, especially noticeable at the exit plane. Figure 2.6 shows the Mach number contours obtained through Rampant. A comparison between the two N-S solutions in Figure 2.5 and Figure 2.6 shows that they are in agreement. The Rampant solution predicts a slightly lower Mach value at the exit plane than VNAP2.

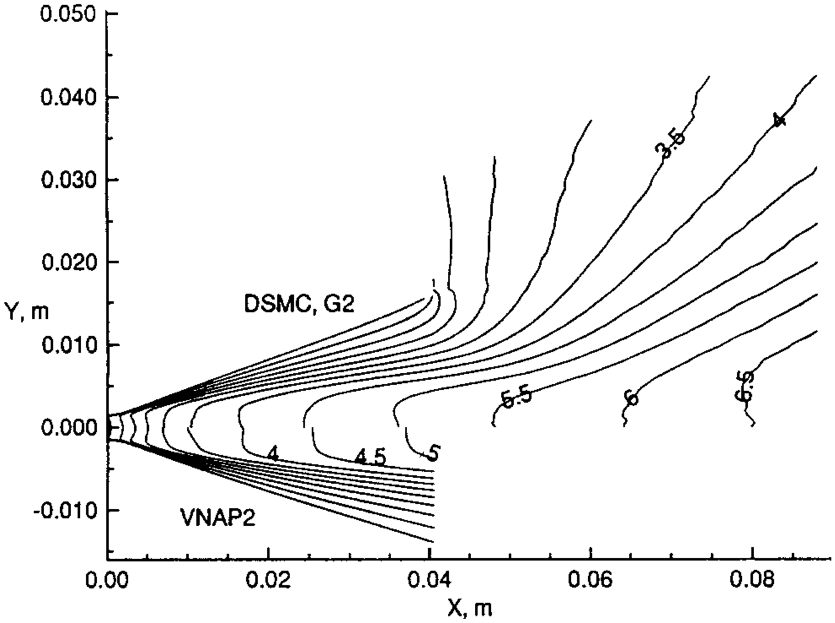

Figure 2.5 DSMC and VNAP2 Mach number contours in the NASA Lewis nozzle (*Tartibini, et al., 1995*).

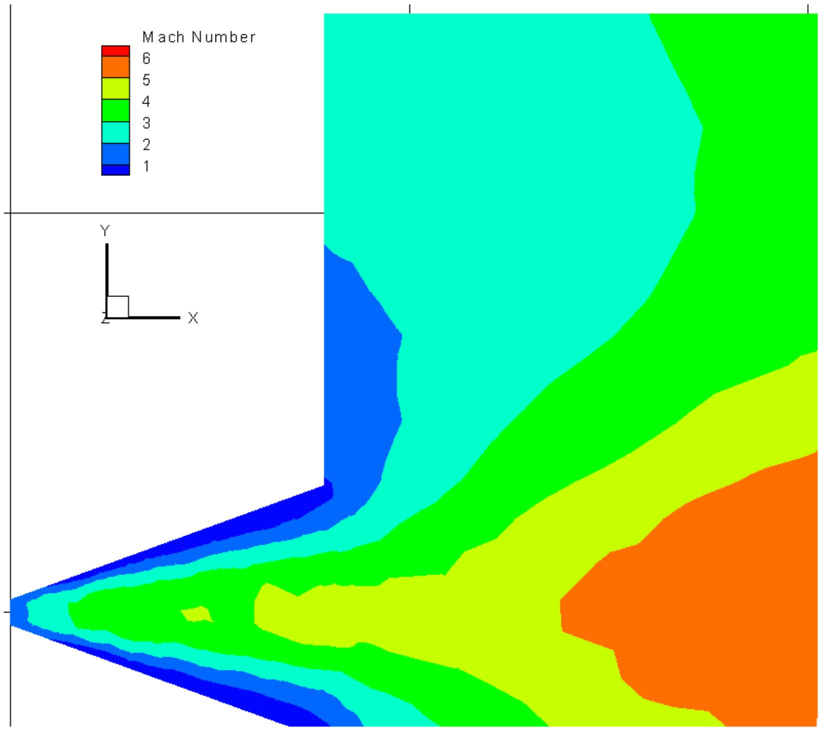

Figure 2.6 Rampant Mach number contours in the NASA Lewis nozzle.

Figure 2.7 shows that the exit velocity profile obtained using Rampant are in good agreement with those of *Tartabini et al*. (1995).

A similar comparison of the temperature profiles in Figure 2.8 shows that Rampant's and VNAP2's results also in agreement with the exception in the core of the flow. Rampant predicts a core flow with a temperature of approximately 40^o K higher than the VNAP2 solution.

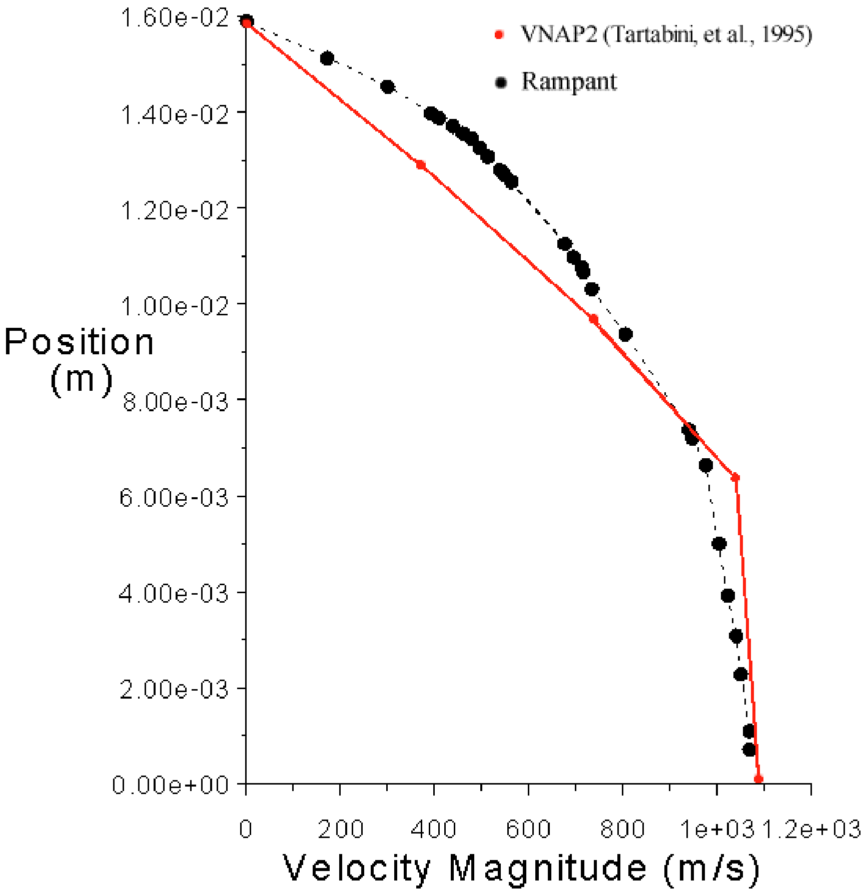

Figure 2.7 NASA Lewis nozzle exit velocity profiles along radial direction.

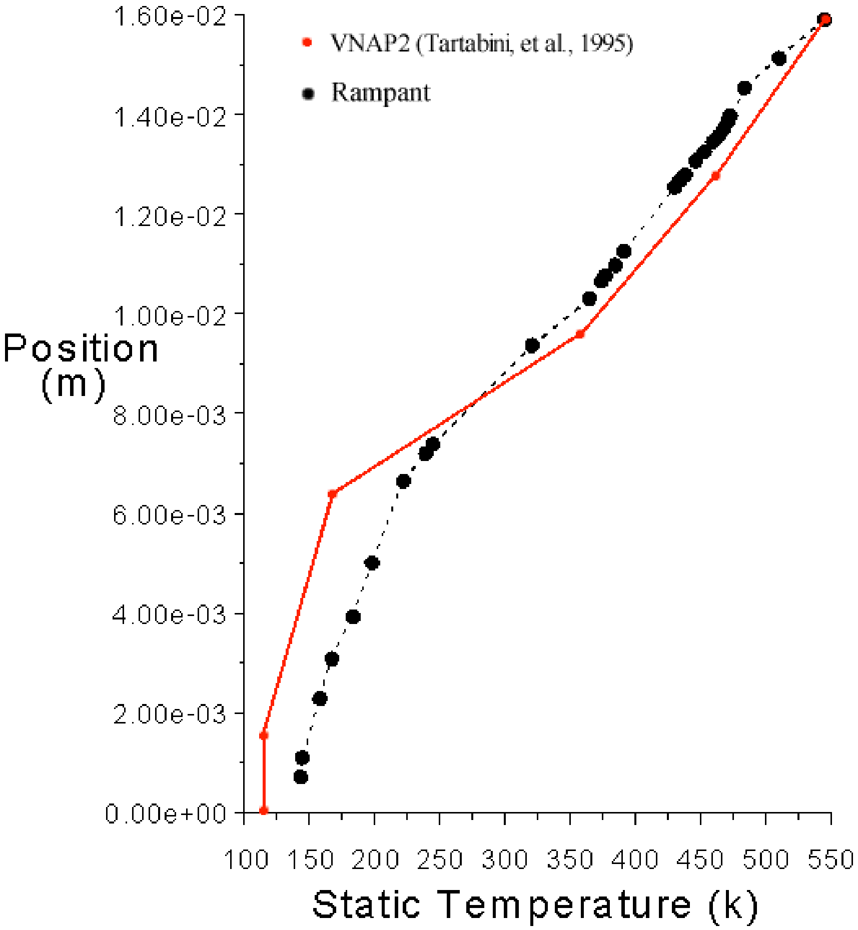

Figure 2.8 NASA Lewis nozzle exit temperature profiles.

2.2.3 Three-Dimensional Nozzle Flow and Comparison to Experimental Data

This validation case presents a comparison between nozzle flow results obtained by Rampant and the experimental data by *Rothe* (1970) that have been used in numerous validation studies as reviewed in the introduction. Rothe used an electron beam technique to measure temperature and density along the centerline of a small nozzle shown in Figure 2.9. The nozzle was operated at various pressures resulting in a range of Reynolds numbers from 110 to 1230. In order to reduce problems associated with rarefaction effects a Re of 1230 was chosen for our simulation and corresponds to a chamber stagnation pressure of 1975 Pa and a stagnation temperature of 300^o K. The wall boundary condition was set as adiabatic in our numerical study as it was maintained during the experimental study. Nitrogen was used as the test gas in our simulation.

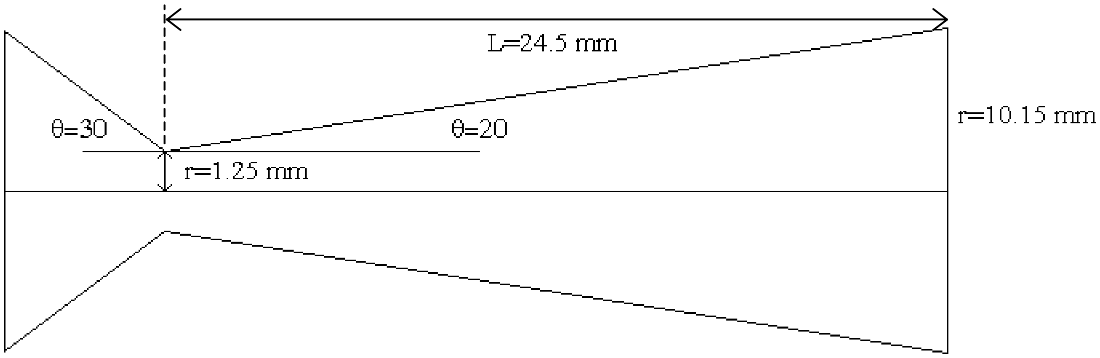

Figure 2.9 Nozzle geometry from Rothe experiment (1970).

Figure 2.10 shows the numerical and experimental temperature profiles normalized to the stagnation temperature of the nitrogen gas along the nozzle centerline. Figure 2.10 demonstrates that Rampant predicts well the experimental data with the exception of the nozzle exit where Rampant predicts a higher temperature. This discrepancy may be attributed to the breakdown of Rampant as the flow reaches a $Kn \cong 0.033$ at the exit plane indicating a rarefied flow condition.

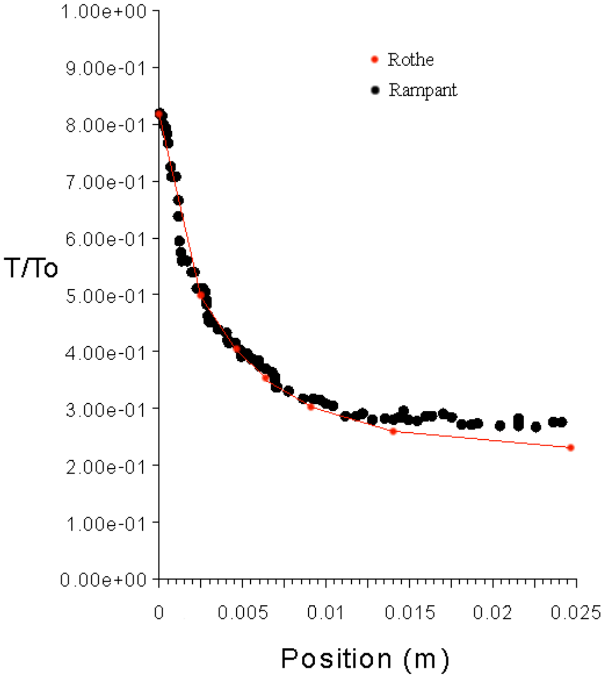

Figure 2.10 Normalized temperature along the centerline of Rothe’s nozzle.

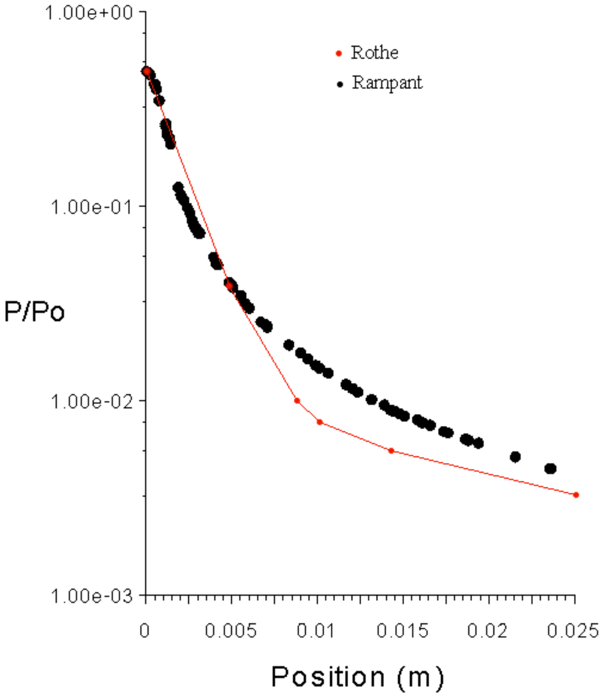

Figure 2.11 Normalized pressure along the centerline of Rothe’s Nozzle.

Figure 2.11 shows the normalized centerline pressure and Figure 2.12 the normalized density. As with the temperature, pressure and density predictions from Rampant are in agreement with Rothe's data.

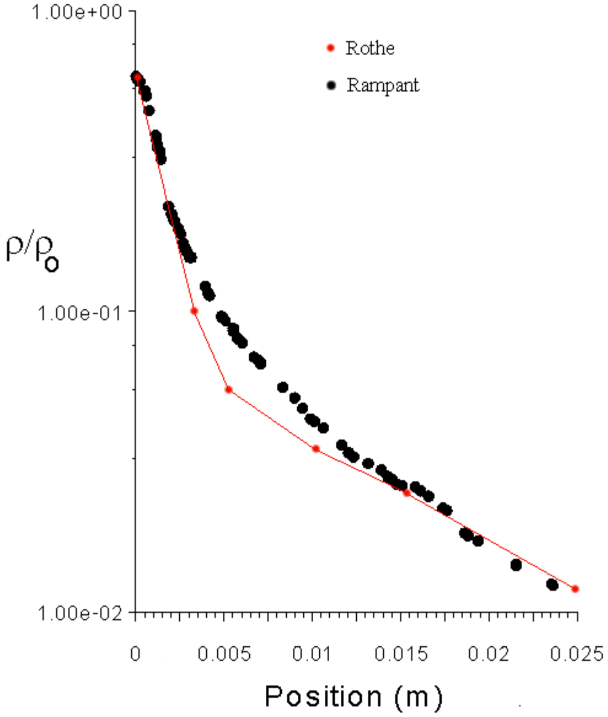

Figure 2.12 Normalized density along centerline of Rothe's nozzle.

The overall good comparisons between Rothe's experiments and computational results indicate that Rampant provides accurate solutions as long as the flow remains within the continuous regime.

2.3 DSMC Methodology and the DAC code

The Direct Simulation Monte Carlo (DSMC) method developed by *Bird* (1994) is used in this study to simulate the rarefied part of the expanding plume flows. In DSMC the flow is simulated using particles that move in the computational domain and collide with other particles and solid surfaces. DSMC uses computational particles that account for many real particles and performs collisions in a Monte Carlo (stochastic) manner. The basic steps in a DSMC code are as follows:

1. The domain is discretized with cells based on the mean free path, λ.
2. Cells are populated with particles based on prescribed distribution functions.
3. Particles enter and leave boundaries based on physical models.
4. Particles move and collide with elastic collision models such as Hard Sphere and Variable Hard Sphere.
5. Particles can also interact in chemical reactions.
6. Particles collide with walls based on specular, diffuse or more complex surface interaction models.
7. Macroscopic quantities such as density and velocity are based on sampling of particle properties.

2.3.1 Grid Generation

The 3-D DSMC code used in this study is DAC, developed at the Johnson Space Flight Center (*Le Beau,* 1997). The DAC code has an advanced grid generation ability that allows complex geometry's to be simulated. Grid generation for the DAC code starts with the surface grid of the solid boundaries found in the computational domain and the input boundary surface. The discretization of the input boundary surface in DAC is based on the mean free path at the location of the boundary surface. Though DAC does not require the input boundary surface grid to be as small as the mean free path, it is better for convergence to generate the grid as refined as possible.

Once the surface grid has been generated and flow parameters from the boundary conditions necessary for the simulation have been set, the generation of the interior flow-field grid is accomplished using PREDAC. This module in DAC generates the interior grid via two methods. The first method sets a free stream value of number density, velocity components, and temperature. The PREDAC utility then creates the interior grid based on the interior surface grid, an exterior box grid, and the mean free path calculated from the input conditions described above. The second method is basically an adaptive grid capability that uses a previous solution to generate a more accurate interior grid. The PREDAC utility calculates the mean free path from the flow-field conditions rather than the free stream conditions. This generates an interior grid that is more efficient in subsequent DAC simulations.

2.3.2 Boundary Conditions

The DAC code allows for four boundary conditions to be set at each surface grid element: wall, out-gassing wall, inflow boundary, and outflow boundary.

The solid wall and out-gassing wall are handled through globally defined variables; fraction of specular reflection, surface catalysis efficiency, and wall temperature. The inflow boundary and the outflow boundary are relatively simple in that they either allow particles to enter or exit the simulation domain respectively. Particles enter the simulation based on the local cell information of number density, velocity components, and temperature.

2.3.3 DAC Flow chart

1. Run SETBC; this utility is used to setup boundary conditions, geometry merging/extractions and rotation/translation.
2. Run PREDAC; a preprocessor to initialize and adapt solutions.
3. Run MOLSCALE; a utility to scale molecule files. Populates that domain more quickly than running several hundred iterations.
4. Run DAC; a code that carries out the DSMC simulation.
5. Rerun steps 2, 3 and 4 until the grid is sufficiently refined.
6. Run DAC until solution is sufficiently converged.
7. Post Processing:

A. Run SPROP: Analyzes surface sample quantities.

B. Run SLICE: Analyzes flow field sample quantities.

2.3.4 Collision Models in DAC

The VHS collision model is utilized by DAC to perform collisions between molecules (*Bird*, 1994). The DAC code can take inputs for the VHS collision model of the viscosity temperature index and the reference temperature.

DAC also handles collisions between molecules and solid surfaces. These collisions require information by the user of the fraction of specularly reflected molecules and the surface temperature of the solid body. The fraction of specularly reflected molecules allows the user to define a specular collision model or a diffuse collision model or some model between the two. The specular collision model is a model that treats the collision between molecules and solid surface as completely elastic while the diffuse collision model treats these interactions as inelastic. For the simulation performed in this thesis the diffuse model was used.

2.3.5 Time Stepping and FNUM's

The time step created by PREDAC is determined by dividing the dimensions of each cell by the average speed of a molecule in that cell. Therefore, each molecule on average spends one time step in each cell. DAC allows the time step to be set manually and in that case it is chosen as a fraction of the PREDAC computed time step. This creates a time step in which each molecule may spend more than one time step in some cells while spending only one time step in other cells.

PREDAC also evaluates an estimate on the average number of real particles per computational particle (FNUM) to be used in the simulation. This also may be set manually. PREDAC attempts to maintain a minimum of 10 molecules in each cell. It does this by refining or coarsening the mesh appropriately and choosing an FNUM sufficient to allow for a reasonable molecule population. The FNUM can be set to some value slightly lower than the calculated value given by PREDAC. This has the affect of increasing the number of particles in each simulation allowing for better statistical sampling at the price of computational speed.

Chapter III

EMP Nozzle and Plume Flow

This chapter presents simulations of small cold-gas attitude control thrusters onboard the suborbital Environmental Monitor Package (EMP) spacecraft. The EMP carried a pressure sensor connected to the outside of the spacecraft with a long tube and recorded pressure spikes during the firings of its cold-gas thrusters. First a review of the EMP mission and collected data is presented. The coupled Navier-Stokes/DSMC methodology is then described. A discussion of the results is presented for each of the Pitch, Yaw and Roll cases. A discussion of the data collected from the EMP spacecraft with comparison to the simulation results is also presented. Due to an over prediction of the results in the first roll case, a second case for the roll thrusters are presented. The results for the second case and the EMP comparison data are also discussed.

3.1 EMP Description and Problem Definition

The Environmental Monitor Package (EMP) was a suborbital spacecraft designed and built by the Applied Physics Laboratory. The EMP was designed to measure the induced environment around the spacecraft through the use of numerous instruments.

Figure 1.1 shows an engineering view of the EMP spacecraft while Figure 3.1 illustrates the mission profile. The spacecraft's attitude control system is shown in detail in Figure 3.2 as well as the axis convention used for the EMP simulation domains. This system was mounted on its base, which included eight N_2 cold gas thrusters: pitch-down (P-D), pitch-up (P-U), yaw-right (Y-R), yaw-left (Y-L), two roll-clockwise ($R\text{-}CC_1$, $R\text{-}CC_2$) and two roll-counterclockwise ($R\text{-}CCW_1$, $R\text{-}CCW_2$). Nozzle characteristics of the EMP thrusters are indicated in Table 3.1. The EMP thruster-firing period occurred during two phases which spanned the time from 500-1400 s (mission elapsed time) of the EMP mission. The first phase occurred in the time period during which the EMP ascended from 1000 km at 500 s, and then reached apogee of 1230 km at 840 s. The second phase involved the descent to 670 km at 1400 s.

A cold-cathode ionization sensor with operating range of 4×10^{-5} Pa to 0.1333 Pa ($\pm$ 15%) was used to monitor the neutral gas pressure surrounding the spacecraft. The neutral pressure was monitored at a pressure sampling rate of 16.67 samples/s with the EMP rotating with a period of approximately 10 s (frequency of 0.1 Hz.) The pressure sensor, housed in the spacecraft was connected to an entrance hole on the surface of the EMP. The tube had a length L_t=0.1 m and diameter D_t=0.022 m. The location of the pressure-sensor tube inlet was approximately 0.11 m off the axis perpendicular to the EMP base and at a plane 0.15 m from the base of the spacecraft as shown in Figure 1.1. *Gatsonis et al.* (1997) presented an analysis of pressure sensor response in the EMP spacecraft during the quiet thruster period of the mission (second phase), while the EMP was recording ram-wake pressure oscillations.

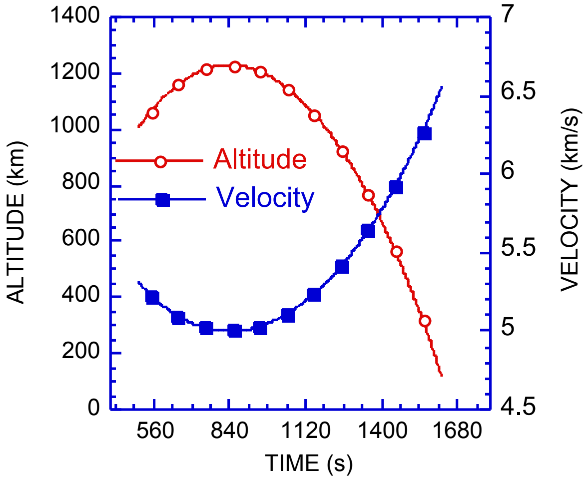

Figure 3.1 Approximate EMP altitude and speed (*Gatsonis et al.*, 2000).

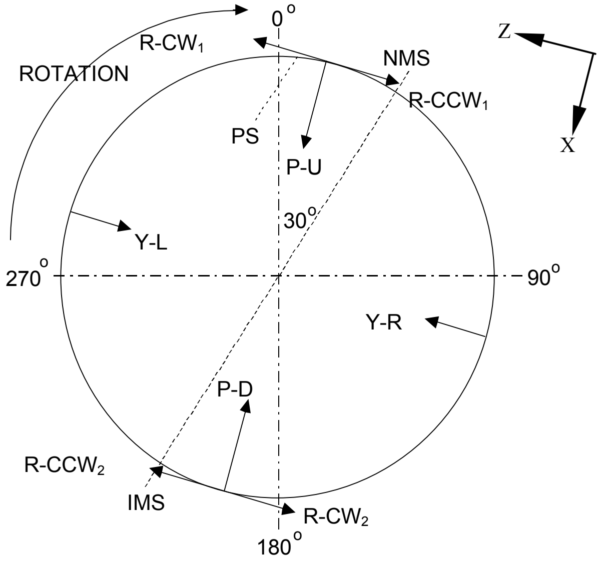

Figure 3.2 EMP base showing thruster location (looking forward, -Y Direction) (*Gatsonis et al.*, 2000).

Thruster	Thrust (N)	Exit Diameter D_e (mm)	Throat Diameter D_t (mm)
Pitch	1.245	4.826	0.906
Yaw	1.245	4.826	0.906
Roll	3.278	5.588	1.6

Table 3.1 EMP thruster characteristics.

A typical pressure profile is shown in Figure 3.3 during thruster firings for the period between 540s and 560s. Data indicates that nearly instantaneous pressure increases are created by all thruster firings. The reduced pressure is obtained by subtracting the background pressure from recorded pressure obtained during the thruster firing.

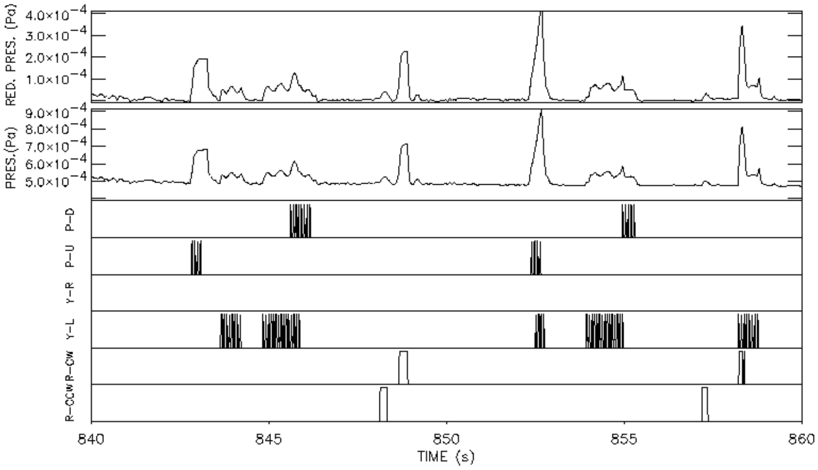

Figure 3.3 EMP data showing the reduced pressure for the 840-860 s thruster-firing period (*Gatsonis et al.*, 1999).

Table 3.2 shows the analysis of individual thruster effects (*Gatsonis et al.*, 1999). The reduced average pressure is the average of the all of the individual thruster firing reduced pressure measurements. This data suggests that similar pressure peaks are not produced even for thrusters of the same thrust levels. The R-CCW thrusters produced pressure amplitudes almost an order of magnitude larger than the R-CW thrusters, while differences between the yaw thrusters are small. The EMP thruster plumes, which did not have a direct line-of-sight to the sensor entrance, result in pressure pulses as shown in Figure 1.2 and Figure 3.3. During the thruster-firing period, the maximum ambient and incident pressure are estimated at approximately $3.7\text{x}10^{-8}$ Pa and $1.7\text{x}10^{-6}$ Pa respectively and occurred at an altitude of 670 km (1400 s). The pressure recorded inside the EMP sensor is orders of magnitude higher than the maximum ambient and incident pressure, as shown in Table 3.2. It can be conclude that for this part of the EMP mission, the effects of the ambient flow are negligible and therefore all pressure measurements can be attributed to the thruster firings. Details of the data analysis can be found in *Gatsonis et al*. (1999).

Thruster	Number of Firings	Reduced Average Pressure (Pa)	Standard Deviation (Pa)
Pitch-Down	27	3.19×10^{-5}	7.73×10^{-6}
Pitch-Up	210	1.3×10^{-4}	3.91×10^{-5}
Yaw-Right	21	4.56×10^{-5}	1.34×10^{-5}
Yaw-Left	1450	5.67×10^{-5}	2.04×10^{-5}
Roll-CW	270	2.09×10^{-4}	7.81×10^{-5}
Roll-CCW	248	1.41×10^{-5}	7.25×10^{-6}

Table 3.2 Reduced average pressure of individual thrusters (*Gatsonis et al.*, 1999).

3.2 Numerical Methodology

Features typical of small cold-gas thrusters (discussed in Chapter 1) are expected to be exhibited by the EMP nozzle and plume flow. Table 3.3 shows estimates of the flow conditions for Reynolds and Knudsen numbers at the throat and exit, which indicate that the EMP nozzle flows are expected to be well within the continuum regime. A rapid expansion due to the flow turning near the nozzle lip is expected to cause rarefaction to be reached quickly. Downstream within the plume, a similar phenomenon is expected from which a surface can be defined where rarefaction effects breakdown the continuous character of the flow. The methodology adapted in our study is summarized as follows:

1. Perform three-dimensional N-S simulations of the nozzle and plume flow until breakdown using a domain that includes the thruster geometry and the necessary EMP surfaces.
2. Perform three-dimensional DSMC simulations for the plume flow in a domain that includes the EMP geometry up to the plane of the pressure sensor. The input surface for the DSMC simulation is inside the breakdown surface as determined by the N-S simulations.
3. The flow conditions at the entrance of the pressure sensor entrance have been used by *Gatsonis et al.* (2000) to obtain the pressure inside the sensor chamber.

Thruster	Throat		Exit	
	Re	*Kn*	*Re*	*Kn*
Yaw/Pitch	635,000	1.75×10^{-6}	26,380	9.4×10^{-5}
Roll	736,000	1.51×10^{-6}	60,400	4.0×10^{-5}

Table 3.3 Estimates of flow conditions at thruster throat and exit.

3.3 Continuous Nozzle and Plume Flows

In this study Rampant (*Fluent*, 1996) is used to obtain the continuous nozzle and plume solutions. As shown in Figure 3.2 the Pitch and yaw thrusters fire toward the center of the EMP base and are also identical in size. The computational domain shown in Figure 3.4a is used to perform three-dimensional simulations of nozzle and plume flows for a pitch (or yaw) thruster. The pitch (or yaw) thruster is located 0.0184 m above the EMP base and fires towards the X-direction. The N-S domain contains the detailed geometry of the nozzle as shown in Figure 3.4b. Preliminary simulations determined that breakdown in the plume of a pitch (or yaw) thruster occurs approximately 0.2 m from the exit. This distance is much smaller than the 0.56-m diameter of the EMP base and therefore, the entire EMP geometry was not included in the N-S simulations. Figure 3.4a shows the pitch (or yaw) domain contains a flat plate with dimension 0.2x0.15 m to represent a small section of the EMP base.

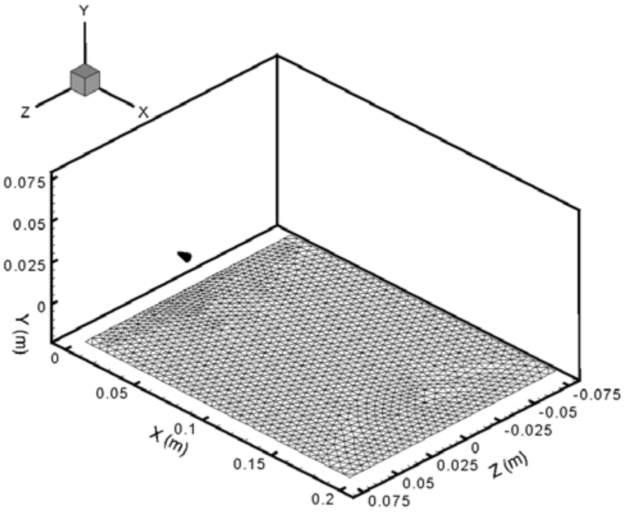

Figure 3.4a) N-S computational domain for nozzle and plume flow. The EMP base is shown as a shaded region. The thruster is located at $(x = 0, y = 0.0184, z = 0)$ and is firing in the +X-direction.

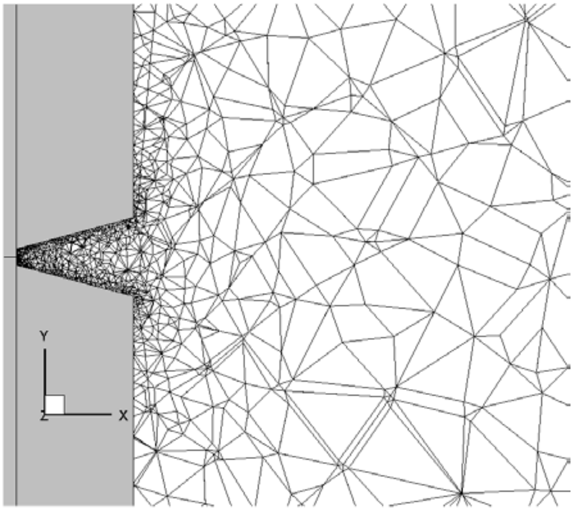

Figure 3.4b) Expanded view of the N-S grid showing the nozzle and near-exit area on the (x,y,z=0) plane. The thruster is located at $(x = 0, y = 0.0184, z = 0)$ and is firing in the +X-direction.

Three-dimensional N-S simulations using Rampant were also performed for the roll thrusters using the domain shown in Figure 3.5a. The Roll thrusters fire in pairs in anti-parallel directions and are located symmetrically on the EMP base as shown in Figure 3.2, but due to a lack of detailed engineering information the exact position of these thrusters is not known. In our first simulation for the roll thrusters, they are placed 0.0184 m above and at the edge of the EMP base as shown in Figure 3.5a. Preliminary simulation showed that the effects of the plume flow over the roll thrusters are confined to only a portion of the EMP base as in the Yaw/Pitch simulation. During the R-CCW firings, only the R-CCW$_1$ thruster, located near the pressure sensor as shown in Figure 3.2, is expected to contribute to the pressure inside the sensor. Similarly, during the R-CW firings, only the R-CW$_1$ thruster is expected to affect the pressure inside the sensor.

By assuming that the effects of the second thruster (R-CCW$_2$ / R-CW$_2$) on the pressure inside the sensor are negligible, the computations can be simplified by including only one roll thruster in the simulations.

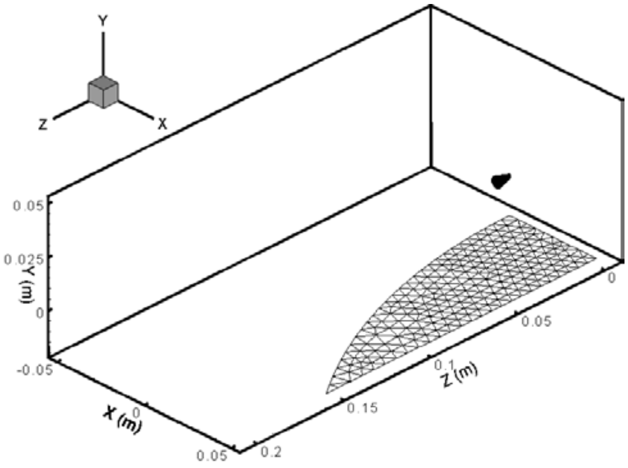

Figure 3.5) N-S computational domain for roll nozzle and plume flow. The EMP base is shown as a shaded region. The roll thruster is located at $(x = 0, y = 0.0184, z = 0)$ **and is firing in the +Z-direction.**

The gas in all the N-S simulations is N$_2$. The flow is modeled from the thruster throat, which is set as the pressure inlet. This point is chosen as the starting location for the simulations because the flow conditions can be specified by analytical equations. The stagnation pressure is set to P_o=1034 kPa; the stagnation temperature is set to $T_o = 300$ ^{o}K. The pressure outlet boundary is set to the ambient at the altitude of the thruster firing. An adiabatic wall condition with a temperature $T_w = 300\,^o$K is used for all solid surfaces.

3.4 Rarefied Plume Flow

The rarefied part of the EMP plume flow is modeled using DAC (*Le Beau*, 1997). The DSMC simulation domain is comprised of the EMP spacecraft up to the plane of the pressure sensor. The DSMC domain for a pitch or yaw thruster is shown in Figure 3.6a. Figure 3.6b shows the DSMC domain for a roll thruster. Figure 3.6a and Figure 3.6b indicate that the DSMC input surfaces are well within the breakdown region of the plume defined as the isosurface of $P \approx 0.03$ from the N-S solution. The input boundary, created from the N-S solution, creates the coupling method between the Navier-Stokes solution and the DSMC simulation. Input data from the N-S solution necessary for the DSMC simulation are produced using linear interpolation and the TecPlot visualization software (*TecPlot*, 1996). Ambient free stream conditions are used for the boundaries of the computational domain. Based on measurements aboard the EMP, the surface is set to a diffuse reflection and surface temperature $T_w = 300$ K.

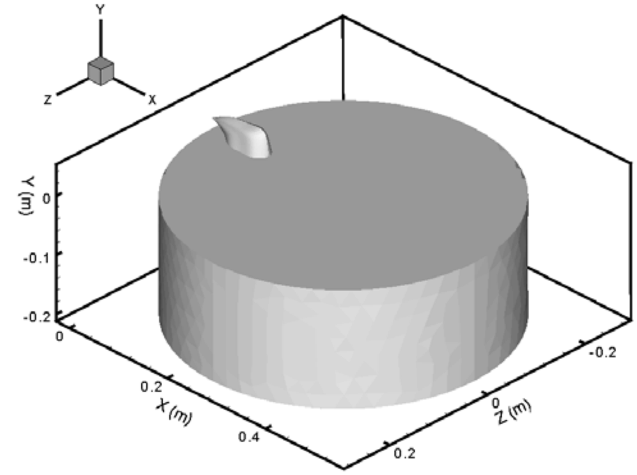

Figure 3.6a) DSMC computational domain for the Yaw/Pitch thruster showing the EMP surface and the DSMC input surface obtained from the N-S simulations. The thruster is located at $(x = 0, y = 0.0184, z = 0)$ and is firing in the +X-direction.

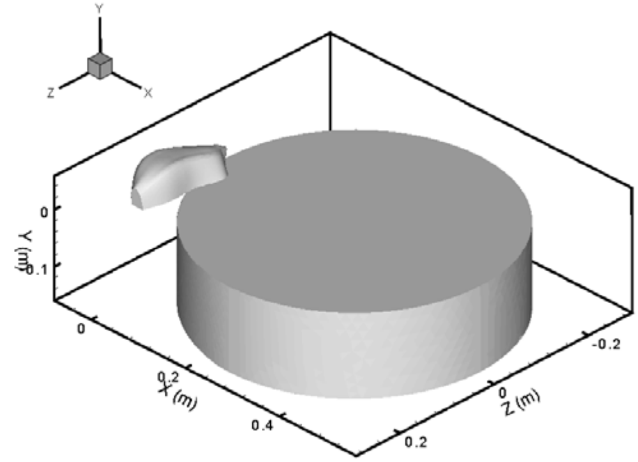

Figure 3.6b) DSMC computational domain for the roll thruster showing the EMP surface and the DSMC input surface obtained from the N-S simulations. The roll thruster is located at $(x = 0, y = 0.0184, z = 0)$ and is firing in the +Z-direction.

The mean-free paths calculated from the N-S solution, and an approximation of the expanding plume for the rarefied part of the domain is used to create the surface grid for the DSMC computations. The interior grid is generated by DAC using mean-free paths based on flow conditions at the DSMC-input surface. This procedure creates a grid that is initially over-refined. Multiple grid adaptations are performed based on the previous DSMC solutions. Once the grid is sufficiently adapted, the solution can be allowed to run until the simulation reaches steady state. It was determined that for the EMP thrusters, the time of thruster operation is larger than the time required for the plume to reach steady state. The EMP thrusters generated multiple impulses that lasted for 0.03 s per impulse. It is also demonstrated in Figure 3.3, as well as by *Gatsonis et al.* (1999) that pressure spikes occurred nearly simultaneously with the firings, which were followed by a gradual decay. All the above suggests that steady-state DSMC results should be sufficient to predict the flow conditions at the entrance of the pressure-sensor tube. Unsteady DSMC calculations would be required in cases where predictions of the pressure evolution were necessary.

3.5 Results and Discussion

3.5.1 Pitch and Yaw Thrusters

The pitch and yaw thrusters are identical in size and fire directly into the middle of the EMP base as shown in Figure 3.4a. The flow characteristics of a typical case can be considered representative of the flow resulting from a pitch (or yaw) thruster. Figure

3.7a, 3.7b and 3.7c display, respectively, the number density, temperature and Mach contours from the N-S simulation for a pitch (or yaw) thruster. The results are plotted on the $(x, y, z = 0)$ plane passing through the nozzle centerline, which is perpendicular to the EMP base. Figure 3.7 (left) shows an expanded view of the flow field covering the nozzle and the near-exit region. Figure 3.7 (Right) show the plane covering the entire computational domain. The flow accelerates from the throat and reaches $\mathrm{M} \approx 5$ near to the exit. The rapid expansion that occurs near the nozzle lip and the formation of a relatively thin boundary layer inside the nozzle is also shown in Figure 3.7. The near-sonic Mach contours, shown in Figure 3.7c (left), emanate from the thruster throat and terminate at the nozzle lip. The flow, expands in the plume region while its temperature and density drop significantly which is shown in Figure 3.7 (right). At a distance of 0.2 m downstream of the exit, the density is $10^{21}\ \mathrm{m}^{-3}$ which is almost three orders of magnitude lower than that of the thruster exit. The interaction of a pitch (or yaw) plume with the EMP base and the formation of a reflecting wave is shown in Figure 3.7 (right).

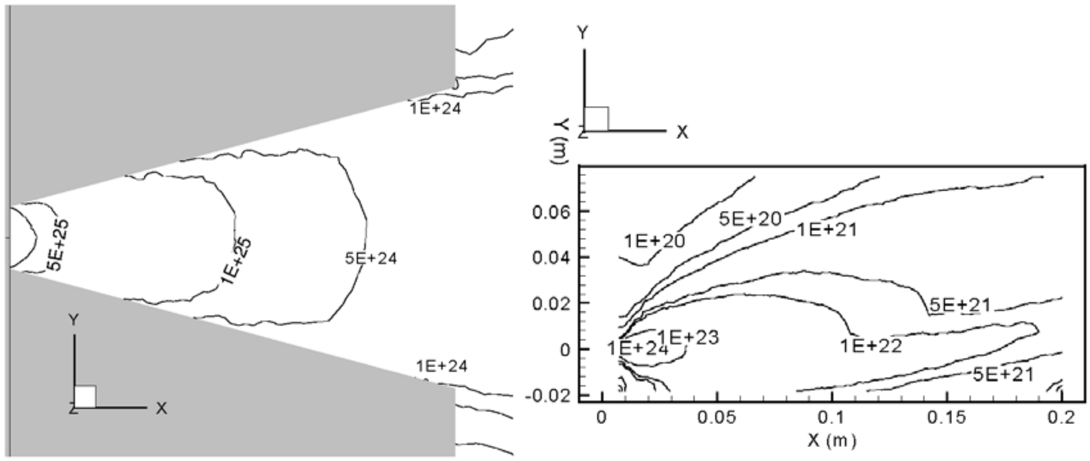

Figure 3.7a) Number density contours (m^{-3}).

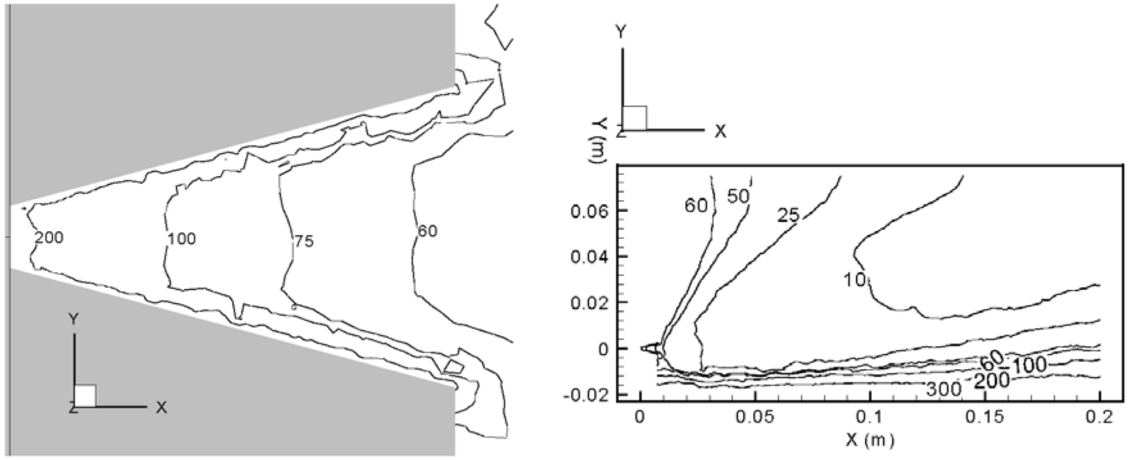

Figure 3.7b) Temperature contours (K).

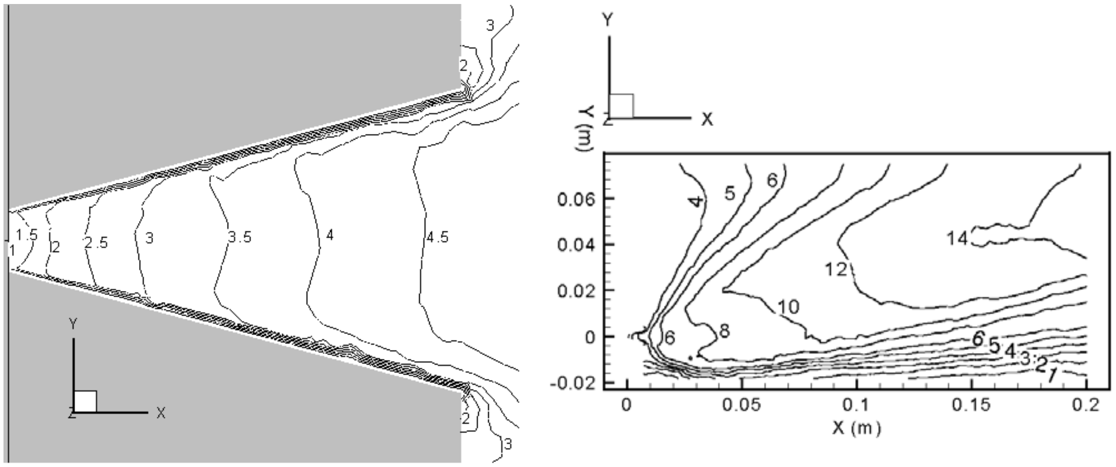

Figure 3.7c) Mach contours.

Figure 3.7 Pitch (yaw) nozzle and plume flowfield from N-S simulations on the (x,y,z=0) plane. (Left) Expanded view of the nozzle and near-exit flow region (Right) Entire domain.

The contours of the breakdown parameter, P are shown in Figure 3.8. The breakdown surface in the Y-direction is asymmetric due to plume-surface interactions. Note that transitional flow does not begin until at least 0.2 m downstream from the nozzle exit.

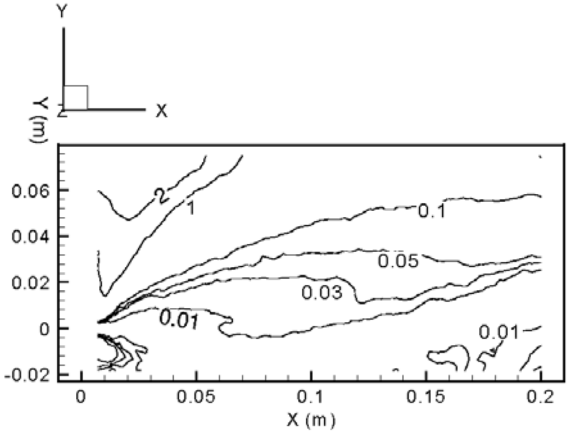

Figure 3.8 Breakdown parameter contours for Pitch (or Yaw) thruster plume from N-S simulation on the (x,y,z=0) plane.

Figure 3.9a shows number density predictions from the DSMC simulation for a pitch (or yaw) thruster. Figure 3.9b shows the $(x, y, z = 0)$ plane, which is perpendicular to the EMP base. This plane passes through the centerline of the EMP pitch/yaw nozzle. Figure 3.9c depicts the thruster plane $(x, y = 0.0184, z)$ passing though the nozzle centerline, which is parallel to the EMP base. Figure 3.9d depicts the $(x, y = -0.15, z)$ pressure-sensor plane, which is also parallel to the EMP base. Figure 3.9b indicates the reflection of the plume flow off the surface of the spacecraft. Figure 3.9b also shows the expansion around the spacecraft edge at the far side of the thruster and the backflow region behind the thruster. The density of the plume flow in the parallel thruster plane (parallel to the EMP base) is symmetric due to the firing orientation of the pitch (or yaw) thruster which can be seen in Figure 3.9c. In the plane of the sensor, the density decreases close to the surface of the EMP and increases in the backflow region of the thruster, which can be seen in Figure 3.9d and Figure 3.9b.

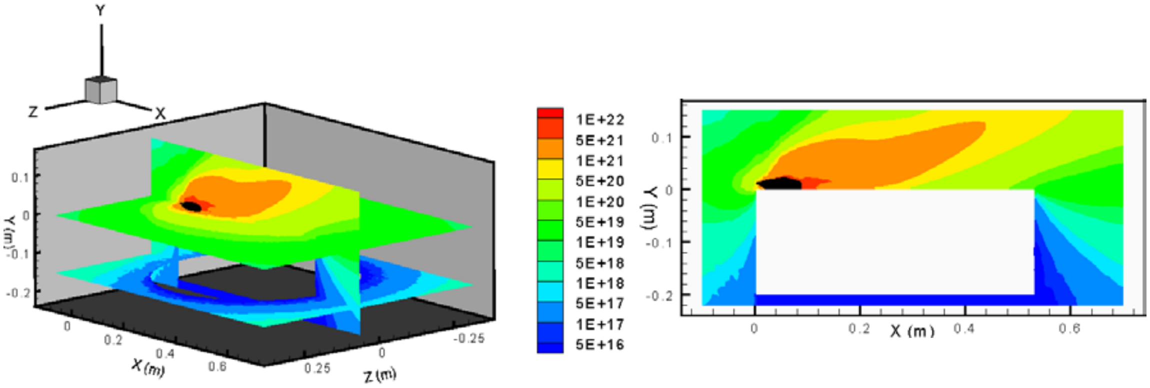

3.9a) Three-dimensional view.

3.9b) Perpendicular thruster plane (x,y,z=0).

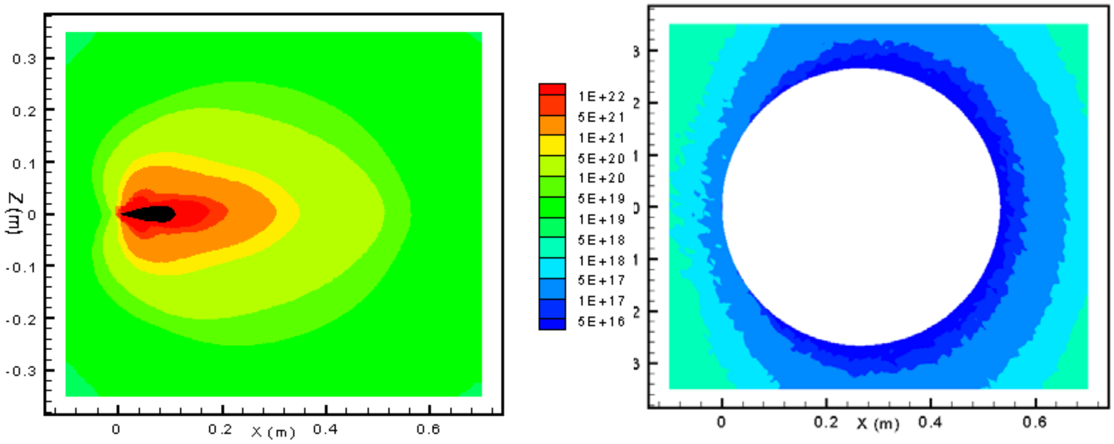

3.9c) Parallel thruster plane (x,y=0.0184 ,z).

3.9d) Pressure sensor plane (x,y=-0.15,z).

Figure 3.9 DSMC number density (m^{-3}) for a pitch (or yaw) thruster plume. The thruster is located at (x=0,y=0.0184,z=0) and is firing in the +X-direction. The DSMC input surface is shown as a black-shaded region.

The EMP surface pressure predicted by DSMC is depicted in Figure 3.10a and Figure 3.10b. The maximum pressure occurs at the base of the spacecraft where the plume impinges and reflects. The pressure decreases rapidly as the plume flow moves across the surface and then over the edge of the EMP base and down to its sides. The pressure contours in the backflow region of the thruster can be seen in Figure 3.10b. It is possible to see from Figure 3.10b there is an increase in surface pressure due to the pitch (or yaw) plume backflow.

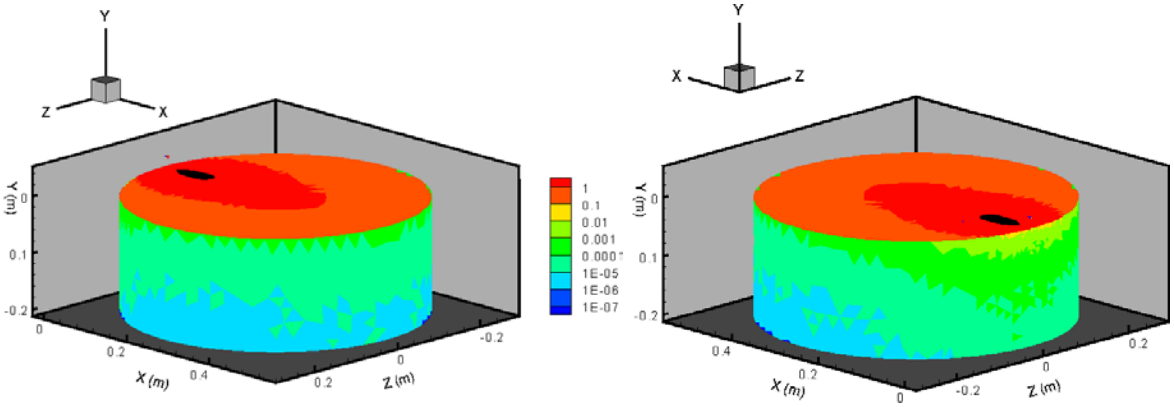

Figure 3.10 DSMC predicted surface pressure (Pa) due to Pitch (or Yaw) thruster plume. The thruster is located at (x=0,y=0.0184,z=0) and is firing in the +X-direction.

3.5.2 Roll Thrusters

The roll thrusters, which are larger than the pitch and yaw thrusters, fire in the Z-direction away from the EMP base (Figure 3.5a). Figure 3.11 shows number density, temperature and Mach from the N-S simulation. The results are plotted on the (*x=0, y, z*) plane passing through the nozzle centerline, which is perpendicular to the EMP base. Figure 3.11 (left) shows the expanded view of the flow field within the nozzle and the near-exit region while Figure 3.11 (right) shows the entire plane of the computational domain. The characteristics inside the nozzle are similar to those of the pitch (and yaw) thrusters. However, due to the partial reflection of the Roll plume off the EMP base, the plume region characteristics are different from those of the pitch (and yaw) thrusters. The plume shown in Figure 3.11 (right), expands while its temperature and density drop significantly due to rarefaction. At a distance of 0.2 m downstream of the exit, the density is approximately $10^{22}\ \mathrm{m}^{-3}$, which is almost three orders of magnitude lower than that at the thruster exit. Figures 3.11a,b,c (right) show that the interaction of the plume with the EMP base results in the formation of a reflecting wave as in the pitch (and yaw) case.

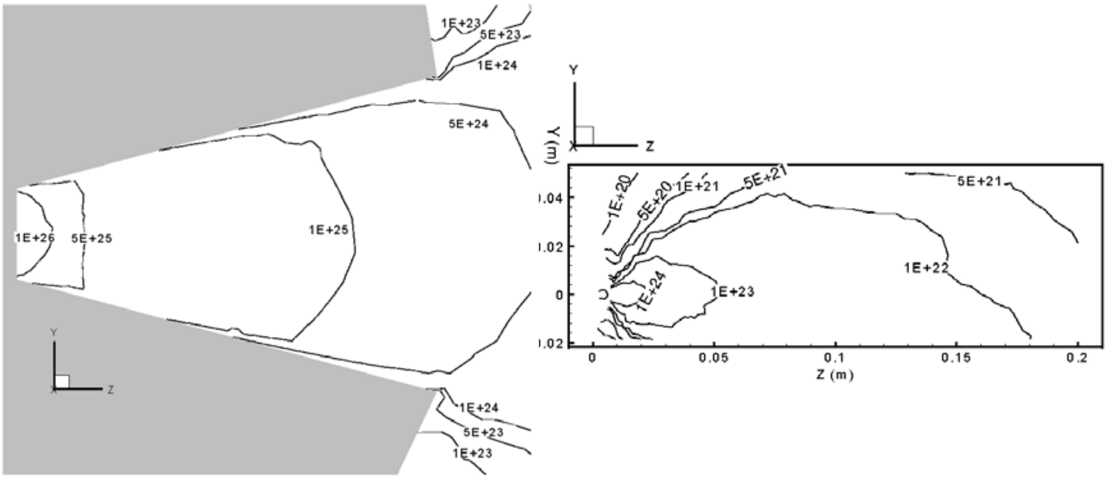

3.11a) Number density contours (m^{-3}).

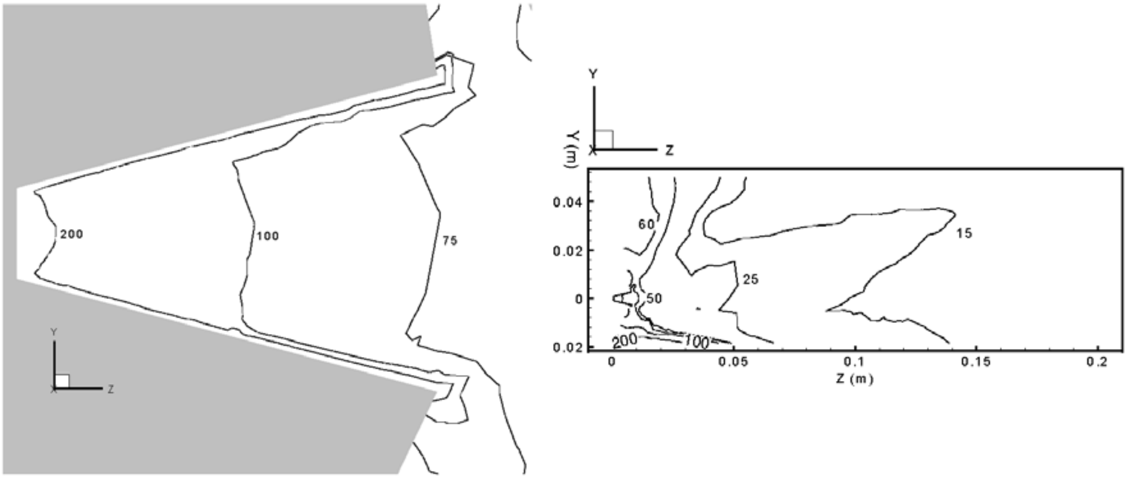

3.11b) Temperature contours (K).

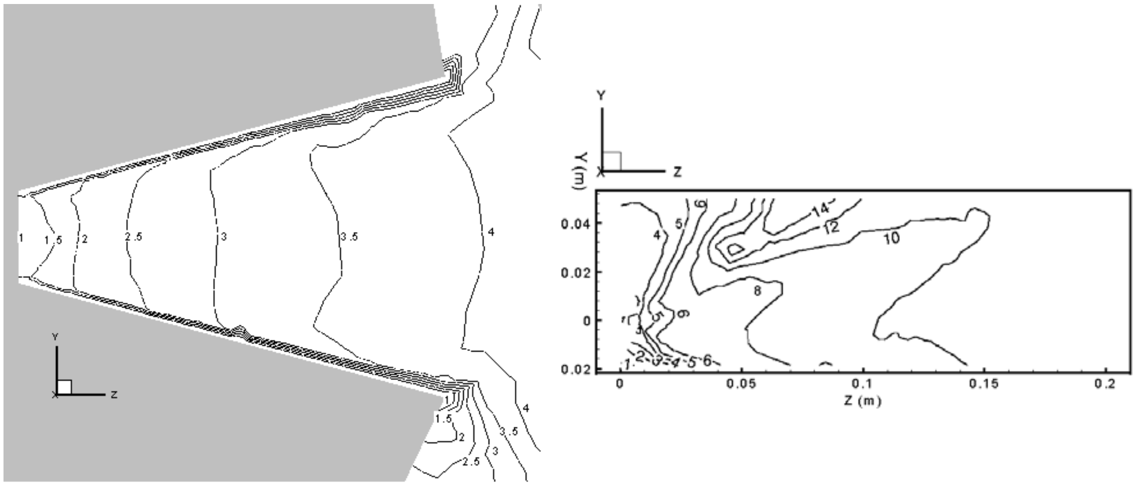

3.11c) Mach contours.

Figure 3.11 Roll nozzle and plume flow field from N-S simulations on the (x,y,z=0) plane. (Left) Expanded view of the nozzle and near-exit region, (Right) Entire domain.

The contours of the breakdown parameter, *P* are shown in Figure 3.12. Plume-surface interaction causes the breakdown surface to be asymmetric. Note that transitional flow does not begin until at least 0.2 m downstream from the exit.

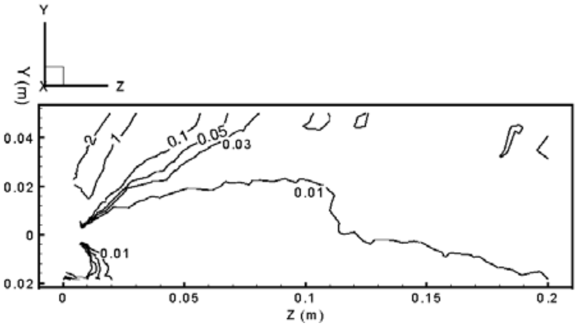

Figure 3.12 Roll nozzle and plume breakdown parameter from N-S simulations shown on the (x,y,z=0) plane.

DSMC number density predictions for a roll thruster are shown in Figure 3.13. The $(x=0, y, z)$ plane that passes through the centerline of the nozzle and is perpendicular to the EMP base is shown in Figure 3.13b. The parallel thruster plane $(x, y=0.0184, z)$ is shown in Figure 3.13c. The $(x, y=-0.15, z)$ pressure-sensor plane parallel to the EMP base is shown in Figure 3.13d. The plume, shown in Figure 3.13b, reflects off the surface of the spacecraft forming a large backflow region. The density at the parallel thruster plane, shown in Figure 3.13c, is asymmetric due to the firing of the roll thruster close to the edge of the EMP base. The pressure-sensor plane, shown in Figure 3.13d, shows that the density perturbation is confined to the roll-thruster side of the EMP.

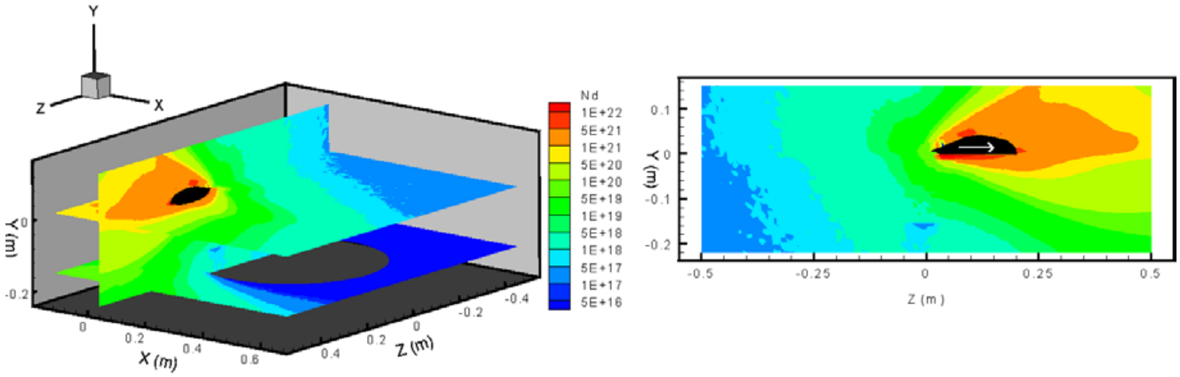

3.13a) Three-dimensional view.

3.13b) Perpendicular thruster plane (x=0,y,z).

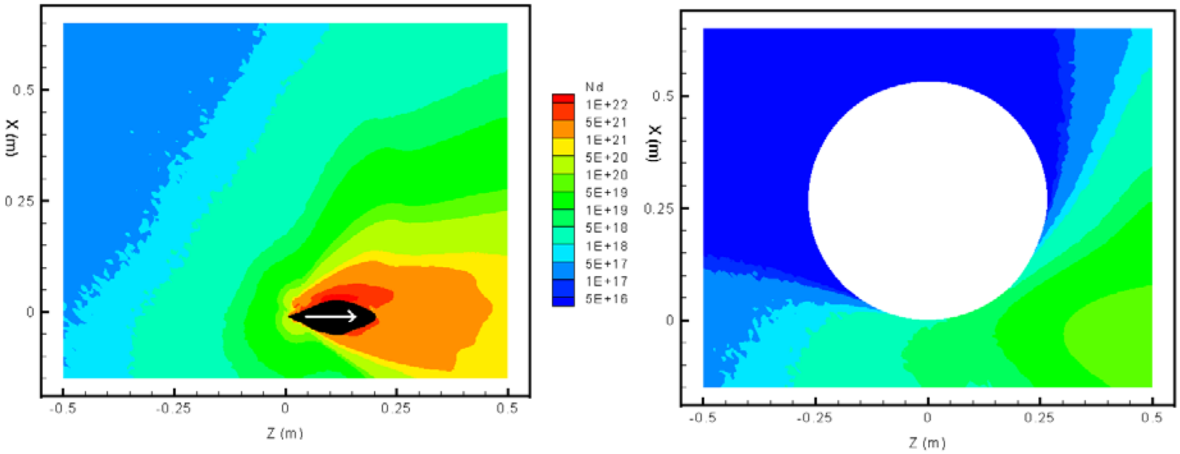

3.13c) Parallel thruster plane (x, y=0.0184, z).

3.13d) Pressure sensor plane (x, y=-0.15, z).

Figure 3.13 DSMC number density (m^{-3}) for Roll thruster plume. The thruster is located at (x=0,y=0.0184,z=0) and is firing in the +Z-direction. The DSMC input surface is shown as a black-shaded region.

Figures 3.14a and 3.14b present the EMP surface-pressure predicted by DSMC. Pressure is higher on the EMP base that is closer to the roll thruster. High surface pressure levels are created when a portion of the roll plume flow expands freely and leaps to the side of the EMP. At the opposite EMP roll thruster side, the pressure is at background levels. This is consistent with our assumption that the roll thrusters although firing in pairs, are not expected to contribute to the EMP surface-pressure equally.

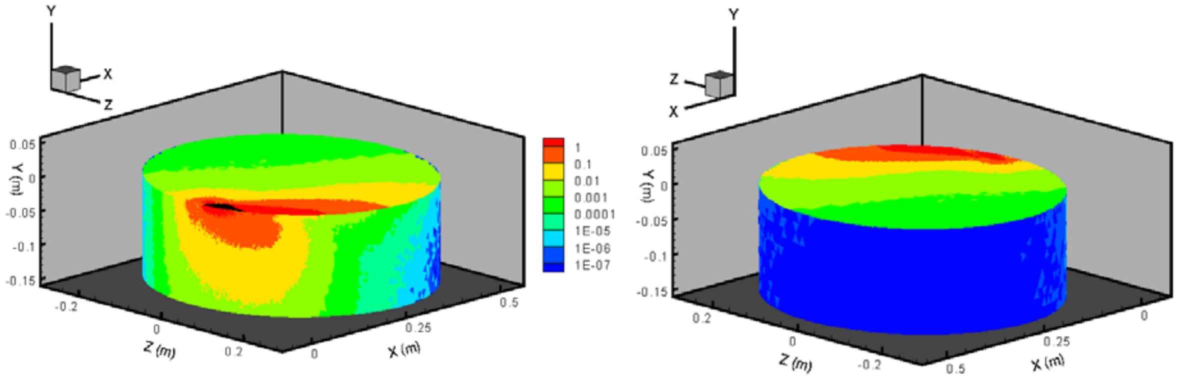

Figure 3.14 DSMC predicted surface pressure (Pa) due to Roll thruster plume. The thruster is located at (x=0,y=0.0184,z=0) and is firing in the +Z-direction.

3.6 Data Comparison

The flow conditions at the surface of the EMP and the entrance of the pressure-sensor tube are obtained by N-S/DSMC computations of the nozzle and plume flows. However, some means of estimating the pressure inside the sensor chamber is needed in order to compare with experimental measurements taken during the EMP mission. The data comparison is presented by *Gatsonis et al.* (2000) and is summarized here. Our

DSMC simulations showed that near the entrance of the sensor tube the plume is in a rarefied state and the flow velocity is nearly parallel to the EMP side surface. Figure 3.15 shows a schematic of the underlying EMP pressure-sensor geometry used by *Gatsonis et al.* (1997, 2000) for the application of the pressure-probe theory of Hughes and de Leeuw. (1965)

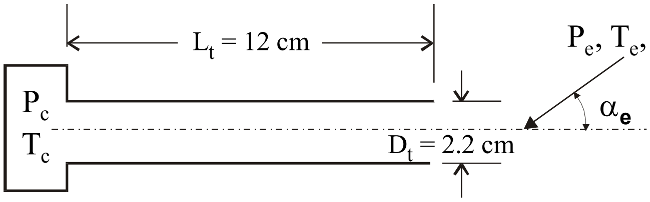

Figure 3.15 Schematic of the EMP pressure-sensor (*Gatsonis et al.*, 1997).

A tube with a ratio $D = D_t / L_t = 0.22$ connects the sensor chamber with the external plume flow incoming at an angle of attack α_E, mean speed U_E, temperature T_E and pressure $P_E = n_E k T_E$. The flow conditions in the sensor chamber are designated by a temperature T_C and the equilibrated pressure inside the volume, $P_C = n_C k T_C$, is written in terms of the pressure ratio $R(S_E, D, \alpha_E)$ by

$$\left(\frac{P_C}{P_E}\right)\left(\frac{T_E}{T_C}\right)^{1/2} = R(S_E, D, \alpha_E) \qquad (3.1)$$

In the above expression, $S_E = U_E / C_{mE}$ is the ratio of the mean speed to the most probable random speed, $C_{mE} = \sqrt{2kT_E / m_E}$. At equilibrium, the flux of molecules that originate in the chamber is equal to the flux entering the tube. This model has been implemented in a computer code (*Maynard*, 1996) and used in *Gatsonis et al.* (1997 & 2000) with input conditions at the tube entrance taken from the DSMC simulations as shown in Table 3.4. The chamber temperature is $T_C = 300\,^{o}$K; and the resulting chamber pressure P_C is shown in Table 3.4.

Thruster	N_E (m^{-3})	T_E (K)	U_E (m/s)	α_E (deg)	P_E (Pa)	P_C (Pa)
P-D	2.07x10^{16}	119	311	87	3.38x10^{-5}	3.8x10^{-5}
P-U	1.20x10^{17}	115	336	84	1.91x10^{-4}	1.98x10^{-4}
Y-R	1.97x10^{16}	87	297	77	2.35x10^{-5}	3.43x10^{-5}
Y-L	2.05x10^{16}	112	246	86	3.16x10^{-5}	3.62x10^{-5}
R-CW (1)	4.13x10^{18}	213	426	80	1.21x10^{-2}	1.47x10^{-2}
R-CCW (1)	3.54x10^{18}	166	505	63	8.08x10^{-3}	2.50x10^{-2}

Table 3.4 Flow conditions at the entrance of the sensor tube and predicted sensor-chamber pressure P_C. Roll thruster position correspond to Case-1.

Figure 3.16 compares the DSMC sensor-chamber pressure predictions correlated from the pressure at the sensor-entrance region, and the EMP reduced average pressure (Average of sensor pressure minus background as shown in Figure (3.3)). The chamber pressures predicted and the measured pressures for the pitch and yaw thrusters are very close. The flux at the entrance of the pressure-sensor tube is mainly due to the random part of the plume flow. Surface geometry and non-equilibrium effects do not play a role as explained in *Gatsonis et al*. (2000).

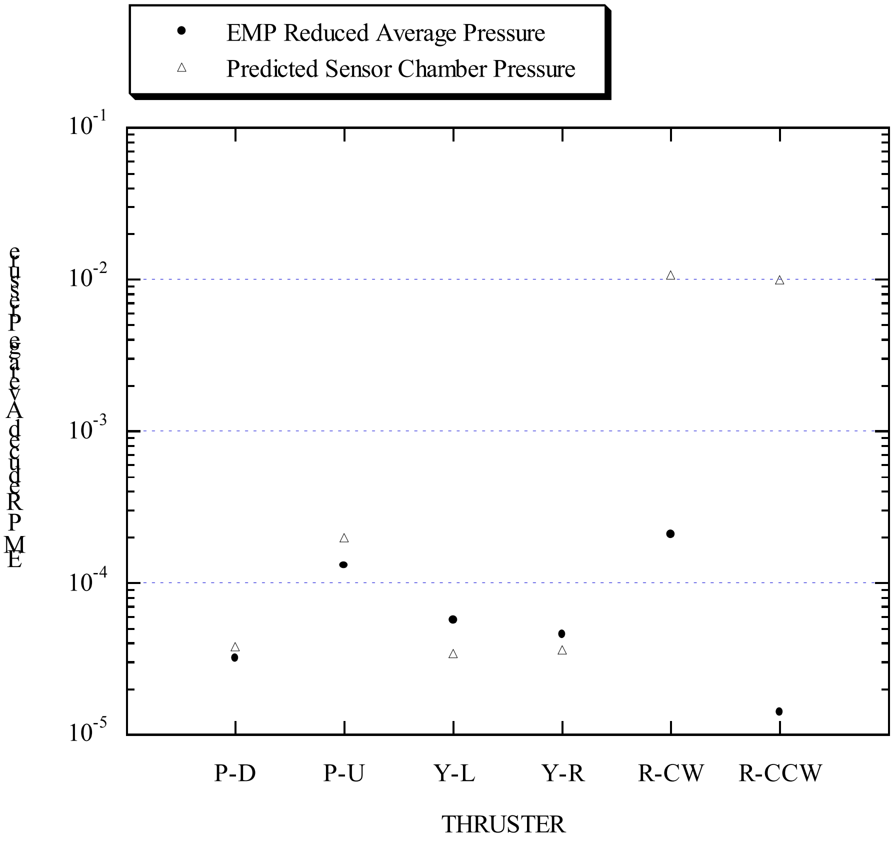

Figure 3.16 Comparison of Numerical and Experimental Pressure for EMP Thrusters. Roll thruster position correspond to Case-1.

An over-prediction of both the R-CCW$_1$ and R-CW$_1$ thrusters is also shown in Figure 3.16. As explained earlier, due to uncertainty in the actual location of the roll thrusters, they were aligned with the EMP edge in our simulations. As a result, a major part of the roll plume reaches the entrance of the pressure-sensor tube directly. In reality, the roll thrusters were located several centimeters inside the edge of the EMP base and their plume underwent expansion on the EMP base before reaching the pressure-sensor entrance. The plume reflection greatly reduced the flux to the sensor tube and, consequently, the pressure inside the sensor. One important conclusion of the roll simulations is that in certain cases the detailed position and geometry of thrusters must be known for accurate predictions.

3.7 Roll Thrusters – Second Case

As a result of the over prediction from the first roll simulation, a second roll thruster simulation was performed in which the thruster location was placed 2.5 cm inside the perimeter of the base surface of the EMP spacecraft. This placement is considered a more realistic approximation to the true geometry of the spacecraft than was simulated in the original roll thruster model. As in the original simulation, the roll thruster still fires in the +Z-direction away from the EMP base (figure 3.5a).

It can be seen by comparing Figures 3.11 and 3.17 that the second roll case plume flow is reflected off of the base surface of the EMP more than in the first roll case. The reflection of the plume flow allows less of the plume flow to reach the pressure-sensor tube. This reduces the chamber pressure found for the second case roll thruster with respect to the first case.

Figure 3.17 shows number density, temperature and Mach from the N-S simulation. The results are plotted on the ($x=0, y, z$) plane passing through the nozzle centerline, which is perpendicular to the EMP base. Figure 3.17 (left) shows the expanded view of the flow field within the nozzle and the near-exit region while Figure 3.17 (right) shows the entire plane of the computational domain. The characteristics inside the nozzle are similar to those of the pitch (and yaw) thrusters. However, due to the partial reflection of the roll plume off the EMP base, the plume region characteristics are different from those of the pitch (and yaw) thrusters. The plume shown in Figure 3.17 (right), expands while its temperature and density drop significantly due to rarefaction. At a distance of 0.2 m downstream of the exit, the density is approximately 10^{22} m^{-3}, which is almost three orders of magnitude lower than that at the thruster exit. Figures 3.17a,b,c (right) show that the interaction of the plume with the EMP base results in the formation of a reflecting wave that is weaker than that in the pitch (and yaw) case.

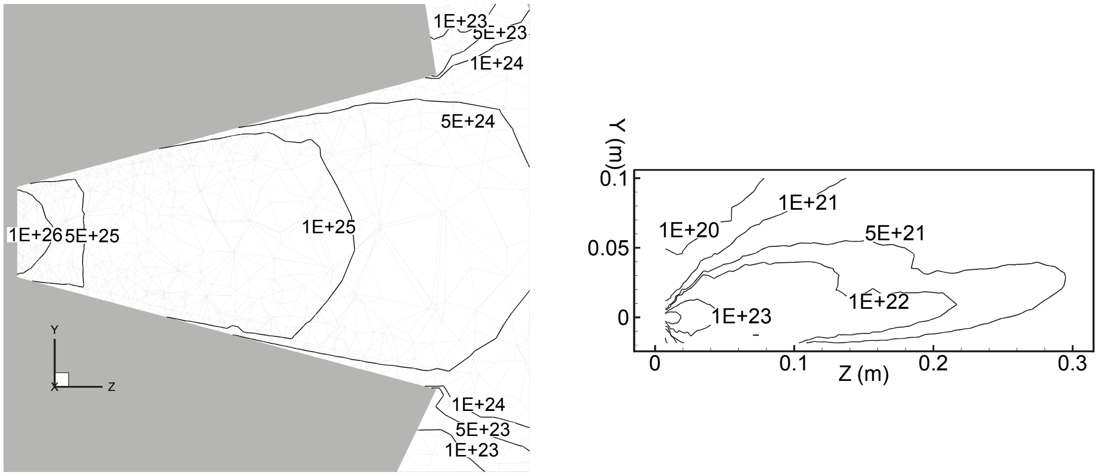

3.17a) Number density contours (m^{-3}).

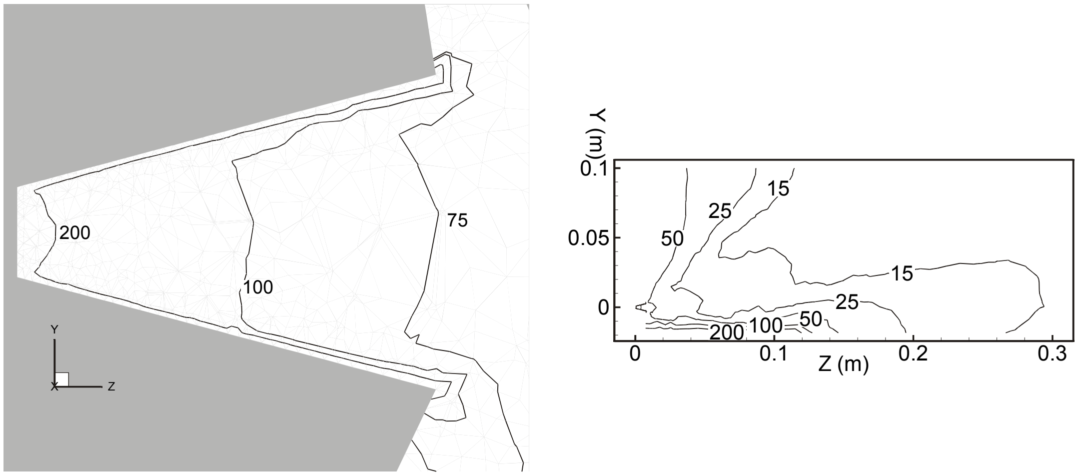

3.17b) Temperature contours (K).

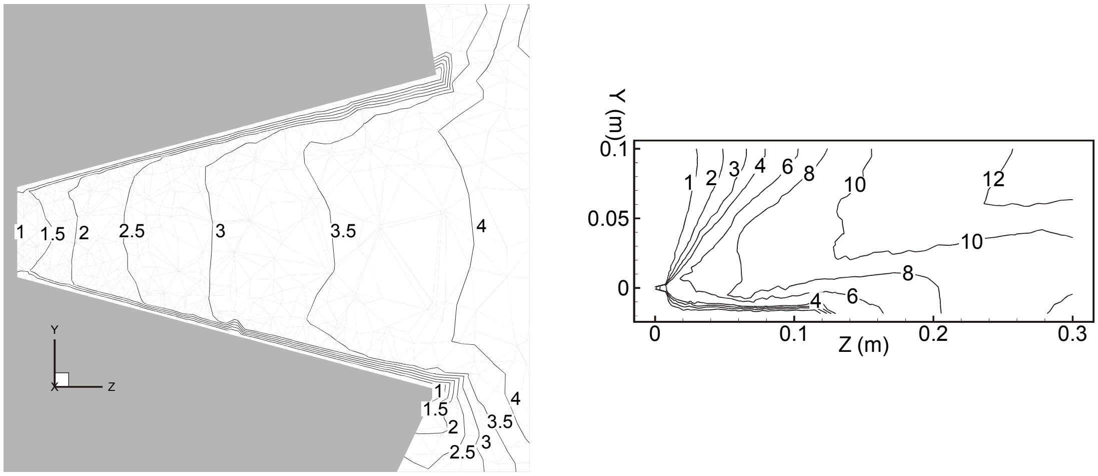

3.17c) Mach contours.

Figure 3.17 Roll nozzle and plume flowfield from N-S simulations on the (x,y,z=0) plane. (Left) Expanded view of the nozzle and near-exit region, (Right) Entire domain.

The contours of the breakdown parameter, *P* are shown in Figure 3.18. Plume-surface interaction causes the breakdown surface to be asymmetric. Note that transitional flow does not begin until at least 0.2 m downstream from the exit.

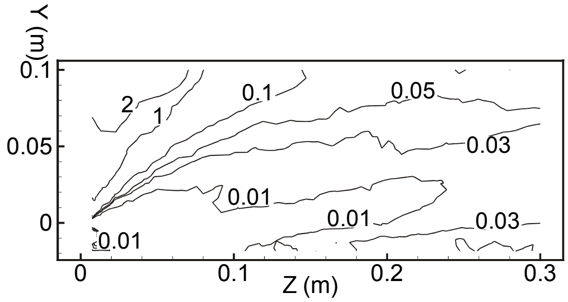

Figure 3.18 Roll nozzle and plume breakdown parameter from N-S simulations shown on the (x,y,z=0) plane.

DSMC number density predictions for a roll thruster are shown in Figure 3.19. The $(x = 0, y, z)$ plane that passes through the centerline of the nozzle and is perpendicular to the EMP base is shown in Figure 3.19b. The parallel thruster plane $(x, y = 0.0184, z)$ is shown in Figure 3.19c. The $(x, y = -0.15, z)$ pressure-sensor plane parallel to the EMP base is shown in Figure 3.19d. The plume, shown in Figure 3.19b, reflects off the surface of the spacecraft forming a large backflow region. The density at the parallel thruster plane, shown in Figure 3.19c, is asymmetric due to the firing of the roll thruster close to the edge of the EMP base. The pressure-sensor plane, shown in Figure 3.19d, shows that the density perturbation is confined to the roll-thruster side of the EMP.

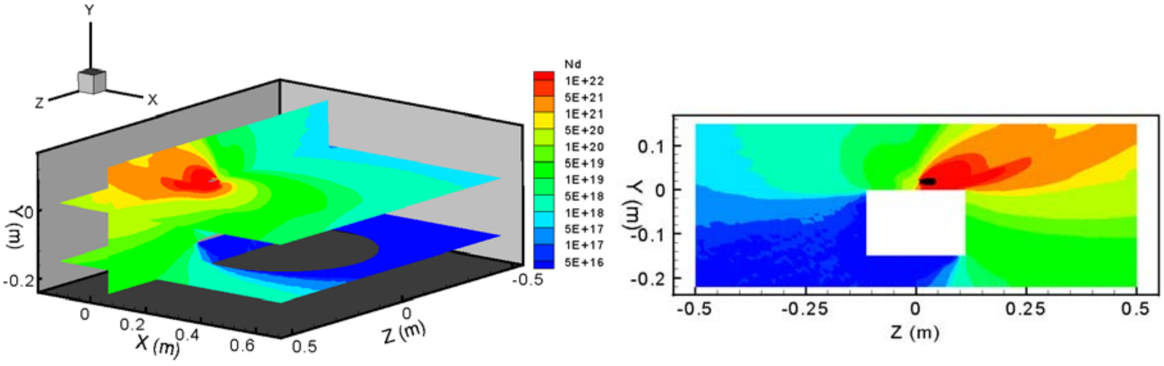

3.19a) Three-dimensional view.

3.19b) Perpendicular thruster plane (x=0,y,z).

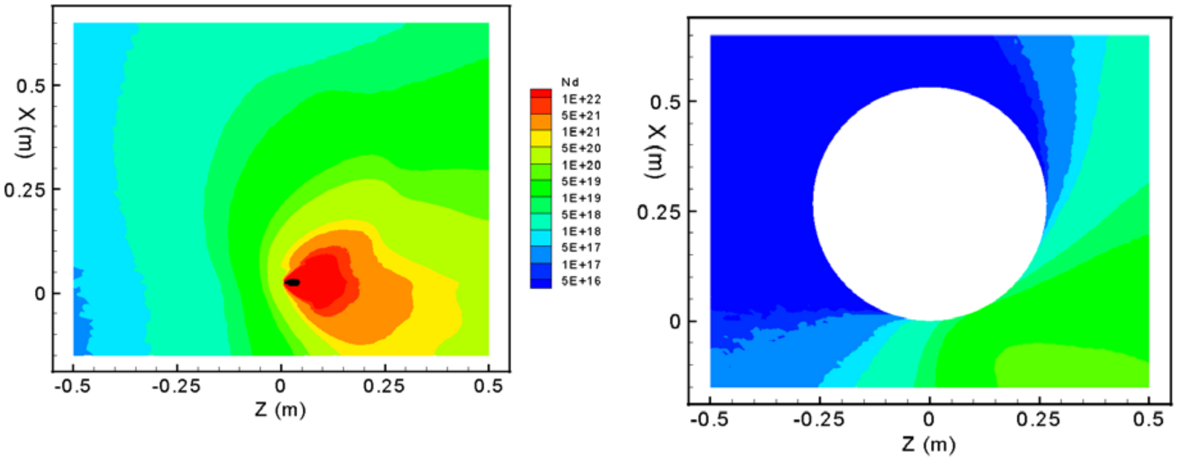

3.19c) Parallel thruster plane (x, y=0.0184, z).

3.19d) Pressure sensor plane (x, y=-0.15, z).

Figure 3.19 DSMC number density (m^{-3}) for Roll thruster plume. The thruster is located at (x=0,y=0.0184,z=0) and is firing in the +Z-direction. The DSMC input surface is shown as a black-shaded region.

Figures 3.20a and 3.20b present the EMP surface-pressure predicted by DSMC. Pressure is higher on the EMP base that is closer to the roll thruster. High surface pressure levels are created when a portion of the roll plume flow expands freely and leaps to the side of the EMP. At the opposite EMP roll thruster side, the pressure is at background levels. This is consistent with our assumption that the roll thrusters although firing in pairs, are not expected to contribute to the EMP surface-pressure equally.

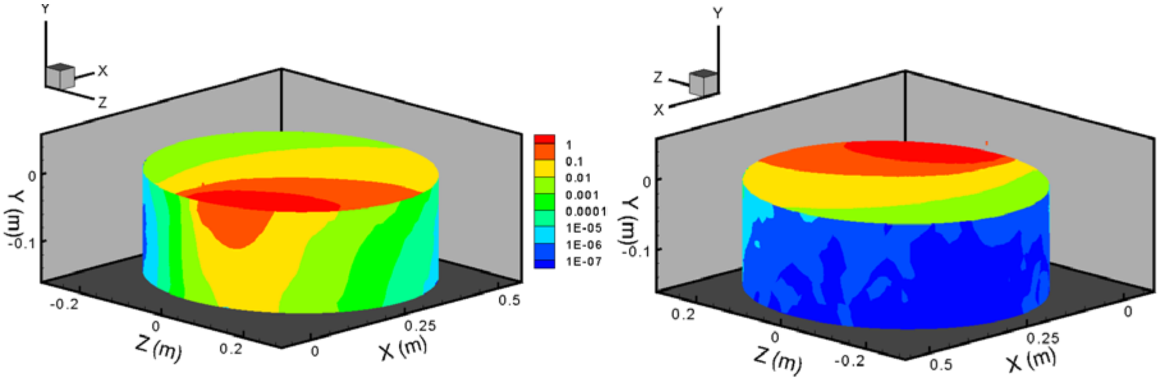

Figure 3.20 DSMC predicted surface pressure (Pa) due to Roll thruster plume. The thruster is located at (x=0,y=0.0184,z=0) and is firing in the +Z-direction.

3.8 Data Comparison –Roll Thruster Cases

The following section presents the results of the second simulation case for the roll thrusters. A comparison of the first and second case is also presented. Input conditions at the tube entrance taken from the DSMC simulations for the first and second case are shown in Table 3.5. It can be seen that an order of magnitude drop in pressure has occurred for the second case over the first roll thruster case. The chamber temperature is $T_C = 300$ ^{o}K; the resulting chamber pressure P_C is shown in Table 3.5.

Thruster (Case)	N_E (m^{-3})	T_E (K)	U_E (m/s)	α_E (deg)	P_E (Pa)	P_C (Pa)
R-CW$_1$ (1)	4.13x10^{18}	213	426	80	1.21x10^{-2}	1.47x10^{-2}
R-CCW$_1$ (1)	3.54x10^{18}	166	505	63	8.08x10^{-3}	2.50x10^{-2}
R-CW$_1$ (2)	1.47x10^{18}	81	571	95	1.64x10^{-3}	1.92x10^{-3}
R-CCW$_1$ (2)	4.78x10^{17}	79	493	81	5.12x10^{-4}	6.33x10^{-4}

Table 3.5 Flow conditions at the entrance of the sensor tube and predicted sensor-chamber pressure P_C due to Roll Thrusters for Case-1 and Case-2 positions.

Figure 3.21 compares the DSMC pressure at the sensor-entrance region, the sensor-chamber pressure predictions and the EMP reduced average pressure. The flux at the entrance of the pressure-sensor tube is mainly due to the random part of the plume flow. Surface geometry and non-equilibrium effects do not play a role as explained by *Gatsonis et al*. (2000).

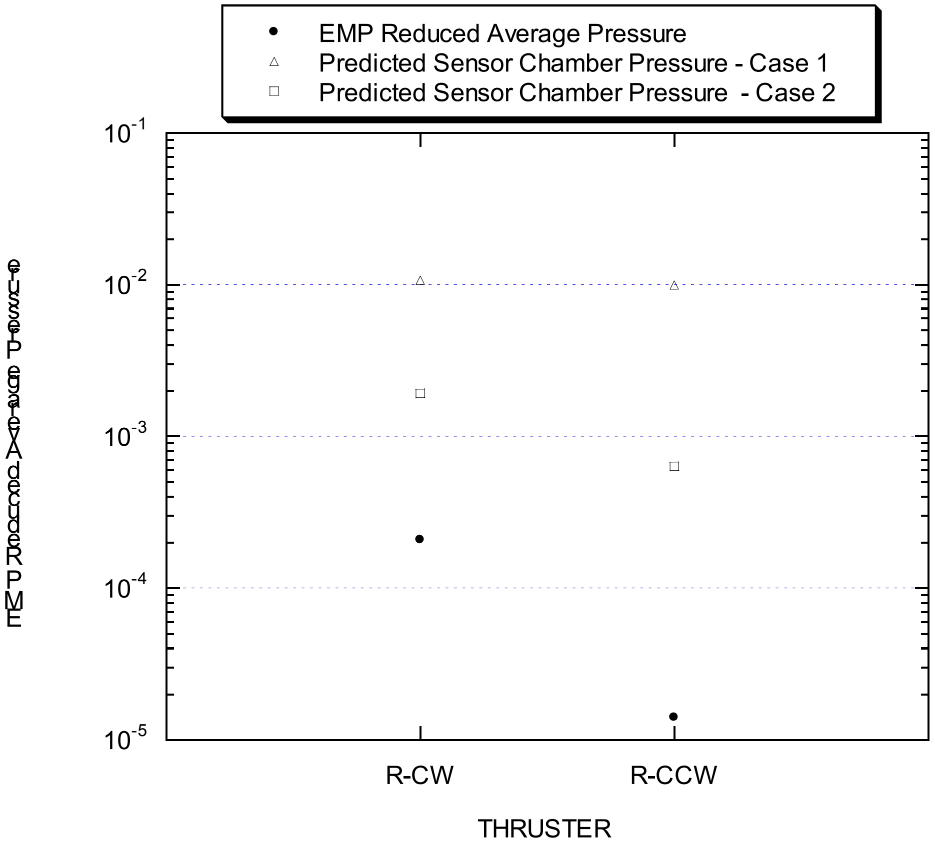

Figure 3.21 Comparison of Numerical and Experimental Pressure for EMP Roll Thrusters for Case-1 and Case-2 Positions.

As explained earlier, in the first case roll thrusters were aligned with the EMP edge in our simulations due to uncertainty in the exact location which resulted in an over-prediction of both the R-CCW$_1$ and R-CW$_1$ thrusters shown in Figure 3.21. It can also be seen that for the second case an over-prediction was also generated though less severe than in the first case. The second case roll thruster was placed 2.5 cm inside the edge of the EMP perimeter based on estimates from limited engineering drawings available.

As a result of the thrusters being placed on the EMP edge for the first case, a major part of the roll plume flow directly reaches the entrance of the pressure-sensor tube. For the second case, less plume flow reaches the pressure-sensor tube. The plume in the second roll thruster case is reflected off of the EMP base away from the pressure-sensor tube. This reduced the chamber pressure for the second case in the pressure-sensor tube.

The flux to the sensor tube, and consequently the pressure inside the sensor, was greatly reduced because the roll thrusters were located inside the EMP base and their plume underwent expansion on the EMP base before reaching the pressure-sensor entrance. One important conclusion of the roll simulations is that the detailed position and geometry of thrusters must be known for accurate predictions. In contrast, the plumes from the Pitch-Down, Pitch-Up, Yaw-Right and Yaw-Left thrusters expand over the entire EMP base diameter of 0.56m before reaching the pressure entrance and are insensitive to this 2.5-cm variation in the position.

Chapter IV

Summary, Conclusions and Future Work

This study involved the modeling of small cold-gas (N_2) thrusters nozzle and plume flows, their interactions with spacecraft surfaces and the induced pressure environment. These small cold-gas thrusters were used for pitch, yaw and roll control and were mounted on the bottom of the conical Environmental Monitor Payload (EMP) suborbital spacecraft. The Pitch and Yaw thrusters had 0.906 mm throat diameter and 4.826 mm exit diameter, while the Roll thrustesr had 1.6 mm throat diameter and 5.882 mm exit diameter. During thruster firing at altitudes between 670 km and 1200 km pressure measurements exhibited non-periodic pulses (*Gatsonis et al*., 1999). The pressure data that motivated this study were taken onboard the EMP, through the use of a pressure sensor onboard the EMP which was housed inside the spacecraft, connected to the outside with a 0.1-m long, 0.022-m diameter tube. The data was collected during the thruster-firing period of the mission with the spacecraft flying from 670 km, to apogee at 1230 km and down to 670 km. Pressure pulses appeared nearly instantaneously with the firings even for thrusters without a direct line-of-sight with the sensor entrance. The pressure pulses also corresponded with the firings for thrusters without a direct line-of-sight with the sensor entrance. Preliminary analysis showed that the plume of these small EMP thrusters undergoes transition from continuous to rarefied, therefore, nozzle and plume simulations are performed using a combination of Navier-Stokes and Direct Simulation Monte Carlo codes. In this study we:

1. Developed a combined 3D Navier-Stokes/DSMC modeling approach using existing codes to study nozzle and plume flows that undergo transition.
2. Validated the Navier-Stokes code with previous numerical and experimental results.
3. Developed a Navier-Stokes/DSMC coupling methodology at the breakdown surface.
4. Applied the combined methodology in the simulation of the cold gas nozzle and plume flows of the EMP spacecraft.

4.1 Numerical Methods and Validation

An overview of the Rampant code used in the continuous simulations is presented in Chapter 2 along with three validation examples.

The first Rampant validation example involved a 2D axisymetric freejet expansion. This case was used to demonstrate the use of Bird's breakdown parameter, *P* and results were compared favorably with those obtained by the method of characteristics from *Bird* (1980). The results confirmed that most of the flow could be modeled using continuous methods and that at distances that are several nozzle diameters downstream breakdown is expected. Both results also demonstrated that in the area near the wall lip, the continuous methods could begin to breakdown due to the rapid plume expansion. The Rampant code did not handle the breakdown of the plume flow as well as the Bird method and showed the flow detaching from the wall lip while the Bird data showed that all Mach numbers contours converged at the wall lip.

The second validation example involved the simulation of a NASA Lewis Research Center nozzle. The nozzle has a throat diameter of 3.18 mm and an exit diameter of 31.8 mm with a half-angle of 20 degrees. Stagnation temperature and pressure were 699 K and 6,400 Pa respectively and the test gas was nitrogen. Three dimensional Rampant simulation results were compared with N-S and DSMC simulations of *Tartabini et al.* (1995). Mach contours, temperature and exit velocity profiles are in agreement with Tartabini et al. for most part of the domain although Rampant's exit mach numbers are slightly lower. Both simulations show that the flow stream becomes rarefied near the nozzle exit.

The third validation example involved three-dimensional simulations of Rothe's (1970) nozzle flow at stagnation temperature of 300 K and pressure of 1975 Pa. Temperature, pressure and density profiles were compared along the centerline of the nozzle flow and agree well with the experimental data of Rothe. The Rampant results overpredict the Rothe data slightly near the nozzle exit. This was attributed to a potential rarefied flow near the nozzle exit that Rampant could not handle.

Overall, Rampant was found to agree well with other modeling techniques as well as with experimental data. The Rampant code showed disagreements with the previous studies and data in cases where the flow became rarefied.

In Chapter 2 the DSMC code DAC used for the rarefied flow simulations was presented. The overview included grid generation, boundary conditions, collision models, time stepping, and particle motion. Validation was not performed for DAC as the code has been previously validated extensively in plume studies.

4.2 EMP Simulations

Chapter 3 presented the EMP thruster simulations. Numerical simulations were performed using a combination of Navier-Stokes and Direct Simulation Monte Carlo (DSMC). For each EMP thruster, the nozzle and plume flow was followed until breakdown using a three-dimensional Navier-Stokes code in a domain that included the detailed geometry of the nozzle and the EMP base. Data from inside the breakdown surface were interpolated and used as inputs to a three-dimensional DSMC plume simulation. The DSMC domain included the EMP spacecraft geometry beyond the plane of the sensor.

The N-S/DSMC simulations showed the complex structure of the plumes including reflections and backflows as they expand over the EMP surfaces. Measurements taken aboard the EMP were compared with chamber pressure predictions. It was shown that the pressure predictions for the pitch and yaw thrusters are very close to the EMP measurements. The plumes of these thrusters reach the pressure sensor after expanding on the EMP base. The pressure due to the roll thrusters is over predicted most likely due to the uncertainty in their location on the EMP base. As a result of their placement at the edge of the EMP base in our simulations, the roll plume does not expand over the 0.56-m diameter base and directly reaches the sensor in the simulations. Further investigation showed that placement of the roll thrusters 2.5 cm inside the edge of the EMP allowed part of the plume to expand over the base and resulted in pressure predictions that are closer to the experimental values. It is therefore concluded that detailed spacecraft geometry and thruster configuration can play a significant part in obtaining accurate results.

4.3 Future Work

A major improvement of current modeling techniques would include methods used to merge the Navier-Stokes with the DSMC codes. The methodology to merge the two codes together in this study was a rather cumbersome process involving the use of several steps. Once the N-S solution was completed it was necessary to perform a calculation to determine the grid structure for the rarefied DSMC simulation. Thus two grids were created independent of each other. Their only connection was the flowfield velocity, temperature and density information.

A truly hybrid code would model the system as one complete geometry by providing only a preliminary mesh. Boundary conditions could be set for the outer bounds of the domain with the breakdown boundary between the continuous and rarefied regimes determined automatically. By merging the two codes into a hybrid program information could be shared between the two domains automatically.

Simulations involving multiple simultaneous thruster firings could also be performed. For example in the EMP case, when using roll thrusters it is necessary to fire at least two thrusters at a time to maintain the stability of the spacecraft. This study was limited to studying single thruster firings. Simultaneous thruster firing could have interesting interactions depending on the placement of the thrusters and the geometry of the spacecraft.

Reference List

Beylich, A.E., Holbeck, H., "Structure of Freejets Issued from Annular Orifices", *AIAA*, 1992.

Bird, G.A., “Breakdown of Translational and Rotational Equilibrium in Gaseous Expansions”, *AIAA Journal*, Vol. 8, No. 11, 1970.

Bird, G.A., “Breakdown of Continuum Flow in Freejets and Rocket Plumes”, *AIAA*, 12th International Symposium on Rarefied Gas Dynamics, 1980.

Bird, G.A., "Molecular Gas Dynamics and the Direct Simulation of Gas Flows", Oxford, 1994.

Blanchard, R.C., "Rarefied-Flow Shuttle Aerodynamics Flight Model", *Journal of Spacecraft and Rockets*, Vol. 31, No. 4, 1994, pp. 550-556.

Boyd I.D., Beattie D.R., Cappelli M.A., "Numerical and Experimental Investigations of Low Density Supersonic Jets of Hydrogen", *Journal of Fluid Mech.*, Vol. 280, 1994 (a), pp. 41-67.

Boyd, I.D., Jafry, Y.R., Beukel, J.V., "Particle Simulations of Helium Micro Thruster Flows", *Journal of Spacecraft and Rockets*, Vol. 31, No. 2, 1994 (b), pp. 271-277.

Boyd, I.D., Jafry, Y.R., Beukel, J.V., “Investiagtion of Nozzle and Plume Expansions of a Small Helium Thruster”, *AIAA*, 1992.

Boyd, I.D., Penko, P.F., Meissner, D.L., DeWitt, K.J., “Experimental and Numerical Investigations of Low-Density Nozzle and Plume Flows of Nitrogen”, *AIAA Journal*, Vol. 30, No. 10, Oct. 1992.

Boyd, I.D., Stark, J.P.W., "Assessment of impingement effects in the isentropic core of a small satellite control thruster", *IMechE*, Vol 203, 1989, pp. 97-103.

Boyd, I.D., VanGilder, D.B., Beiting, E.J., "Computational and Experimental Investigations of Rarefied Flows in Small Nozzles", *AIAA Journal*, Vol. 34, No. 11, 1996, pp. 2320-2326.

C. D. Brown, ‘Spacecraft Propulsion’, *AIAA*, 1996.

Campbell, D.H., "DSMC Analysis of Plume-Freestream Interactions and Comparison of Plume Flowfiled Predictions with Experimental Measurements", *AIAA 26th Thermophysics Conf*, AIAA 91-1362, 1991.

Chung, C.H., De Witt, K.J., “DSMC and Continuum Analysis of Low-Density Nozzle Flow”, *AIAA* 93-0727, 1993.

Dettleff, G., Boettcher, R.D., Dankert, C., Koppenwallner, G., Legge, H., "Attitude Control Thruster Plume Flow Modeling and Experiments", *Journal of Spacecraft and Rockets*, Vol. 23, No. 5, 1985, pp. 476-481.

Dettleff, G., Plahn, K., “Experimental Investigation of Fully Expanded free Jets and plumes”, *21st Intenational Symposium on Rarefied Gas Dynamics*, 1998.

Draper, J.S., Hill, J.A.F., "Rarefaction in Underexpanded Flows", *AIAA Journal*, Vol. 7, 1969.

Dupuis, D., "Monte Carlo Simulation of Plume Effect on Space Vehicles", *AIAA*, 1992.

Fluent Inc. Computational Fluid Dynamics Software, “Fluent/UNS & Rampant”, Release 4.0, April 1996.

Gatsonis, N.A., Maynard, E.P., Erlandson, R.E., "Monte Carlo Modeling and Analysis of Pressure Sensor Measurements During Suborbital Flight", *Journal of Spacecraft and Rockets*, Vol. 34, No. 1, Jan-Feb 1997.

Gatsonis, N.A., Nanson, R.A., Le Beau, G.J., “Simulations of Cold-Gas Nozzle and Plume Flows and Flight Data Comparisons”, Vol. 37, No. 1, *Journal of Spacecraft and Rockets*, 2000.

Gatsonis, N.A., Erlandson, R.E., Swaminathan, P.K., Kumar, C.K., “Analysis of Pressure Measurements During Cold-Gas Thruster Firings Onboard a Suborbital Spacecraft”, in press, *Journal of Spacecraft and Rockets*, Vol. 36, No. 5, 1999, pg. 688-692.

Genkin, L., Baer, M., Falcovitz, J., “Gasdynamics Approach to Small Plumes Computation", *Journal of Spacecraft and Rockets*, Vol. 31, No. 4, 1994, pp. 601-700.

Gilmore, M.R., Gallis, M.A., Harvey, J.K., "Breakdown of Continuum Solvers in Rapidly Expanding Flows", *30th AIAA Thermophysics Conference*, AIAA 95-2134, 1995.

Hill, J.A.F., Draper, J.S., "Analytical Approximation for the Flow from a Nozzle into a Vacuum", *Journal of Spacecraft and Rockets*, Vol. 3, 1966.

Hughes, P.C., de Leeuw, J.H., “Theory for the Free Molecule Impact Probe at an Angle of Attack”, *Rarefied Gas Dynamics*, Vol. 1, Academic, New York, 1965, pp. 653-676.

Hurlbut, F.C., "Particle Surface Interaction in the Orbital Context: A Survey", *AIAA*, 1989.

Ivanov M.S., Markelov G.N., Kashkovsky A.V., Giordano D., “Numerical Analysis of Thruster Plume Interaction Problems”, ESPC 97-A5/3, 2nd European Space propulsion Conference, May, 1997.

Ivanov, M.S., Markelov, G.N., Gerasimov, Yu.I., Krylov, A.N., Mishina, L.V., Sokolov, E.I., “Free-flight Experiment and Numerical Simulation for Cold Thruster Plume” AIAA Paper 98-0898, Jan. 1998.

Koppenwallner G., "Aerodynamics of Rarefied Gases and High-Altitude Flight" AIAA, 1993.

Le Beau, G.J. “The DAC Series: Preprocessor – Run Code – Postprocessors”, *NASA JSC*, Revision 95v1, 1997.

Legge, H., and Dettleff, G., “Pitot pressure and Heat Transfer Measurements in Hydrazine Thruster Plumes”, *Journal of Spacecraft and Rockets*, Vol. 23, No. 4, 1986.

Liang, S.M., Huang, K.L., Chen, K.C., "Numerical Study of Low-Thrust Nozzles for Satellites", *Journal of Spacecraft and Rockets*, Vol. 33, No. 5, 1996, pp. 693-699.

Lumpkin III, F.E., Le Beau, G.J., Stuart, P.C., “A CFD/DSMC Analysis of Plumes and Plum Impingement During Shuttle/Mir Docking”, *AIAA*, AIAA 95-2034, 1995.

Lumpkin III, F.E., Le Beau, G.J., Stuart, P.C., “Enhanced Analysis of Plume Impingement During Shuttle-Mir Docking Using a Combined CFD and DSMC Methodology”, *AIAA*, AIAA 96-1877, 1996.

Maynard, E., "*Direct Simulation Monte Carlo Analysis of Rarefied Gas Flows in Tubes*," MS Thesis, WPI, April 1996.

Meyer, J.T., "Measurements of Particle Densities and Flow Directions in Freejets and in Background Gas", *AIAA*, 1992.

Mombo-Caristan, J.C., Phillippe, L.C., Chidiac, C., et al., "Measurements of Freejet Densities by Laser Beam Deviation", *AIAA,* 1989.

Moore, B.C., Mogstad, T.S., Huston, S.L., Nardacci, Jr. J.L., "Backscatter Contamination Analysis", *AIAA*, 1989.

Moss, J. N., and Bird, G.A., "Monte Carlo Simulations in Support of the Shuttle Upper Atmospheric Mass Spectrometer Experiment", *Journal of Thermophysics*, Vol. 2, No. 2, 1988, pp. 138-144.

Naumann, K.W., "Plume Shape Optimization of Small Attitude Control Thrusters Concerning Impingement and Thrust", *AIAA*, 1988.

Nelson, D.A., Doo, Y.C., "Simulation of Multicomponent Nozzle Flows Into A Vacuum", AIAA, 1989.

Pickett, J.S., Morgan, D.D., Merlino, R.L., "Payload Environment and Gas Release Effects on Sounding Rocket Neutral Pressure Measurements", *Journal of Spacecraft and Rockets*, Vol. 33, No. 4, 1996.

Rault, D.F.G., "Efficient Three-Dimensional Direct Simulation Monte Carlo for Complex Geometry Problems", *AIAA*, 1993.

Rault D.F.G., “Methodology for Thruster Plume Simulation and Impingement Effects Characterized Using DSMC,” *AIAA* 95-2032, 30th AIAA Thermophysics Conference, June, 1995.

Rothe, D.E., "Electron-Beam Studies of Viscous Flow in Supersonic Nozzles", *AIAA Journal*, Vol. 9, No. 5, 1971, pp. 804-811.

Rothe, D.E., “Experimental Study of Viscous Low-Density Nozzle Flow”, AI-2590-A-2, Cornell Aeronautical Lab., Inc., Buffalo, New York, 1970.

Schabram, R.G., Beylich, A.E., Kudriavtsev, E.M., "Experimental Investigation of Co2 and N20 Jets Using Intracavity Laser Scattering", *AIAA*, 1989.

Simons, G.A., “Effects of Nozzle Boundary Layers on Rocket Exhaust Plumes*”, AIAA Journal*, Vol. 10, pp. 1534-1535, 1972.

Tartabini, P.V., Wilmoth, R.G., Rault, D.F.G., “Direct Simulation Monte Carlo Calculation of a Jet Interaction Experiment”, *Journal of Spacecraft and Rockets*, Vol. 32, No. 1, Jan-Feb 1995.

TecPlot, Amtec Engineering, Inc., Version 7, August 1996.

Teshima, K., "Structure of Supersonic Freejets Issuing from a Rectangular Orifice", *AIAA*, 1993.

Wolf, E., Von Zahn, U., “The Shuttle Environment: Effects of Thruster Firings on Gas Density and Composition in the Payload Bay”, *J. Goephys. Res.*, 91:3270-3278, 1986.

Zelesnik, D., Micci, M.M., Long, L.N., “DSMC Simulation of Low Reynolds Number Nozzle Flows”, *AIAA*, AIAA 93-2490, 1993 (a).

Zeleznik, D., Penko, P.F., Boyd, I.D., “Effects of Nozzle Geometry on Plume Expansion for Small Thrusters”, *IEPC*, IEPC 93-135, 1993 (b).